

Voluntary control of semantic neural representations by imagery with conflicting visual stimulation

Ryohei Fukuma^{1,2,3}, Takufumi Yanagisawa^{1,2,3,4,*}, Shinji Nishimoto^{5,6}, Hidenori Sugano⁷, Kentaro Tamura⁸, Shota Yamamoto¹, Yasushi Iimura⁷, Yuya Fujita¹, Satoru Oshino¹, Naoki Tani¹, Naoko Koide–Majima^{5,6}, Yukiyasu Kamitani^{2,9}, Haruhiko Kishima^{1,4}

¹Department of Neurosurgery, Graduate School of Medicine, Osaka University, Suita, Japan

²ATR Computational Neuroscience Laboratories, Seika-cho, Japan

³Institute for Advanced Co-Creation Studies, Osaka University, Suita, Japan

⁴Osaka University Hospital Epilepsy Center, Suita, Japan

⁵Center for Information and Neural Networks (CiNet), National Institute of Information and Communications Technology (NICT), Suita, Japan

⁶Graduate School of Frontier Biosciences, Osaka University, Suita, Japan

⁷Department of Neurosurgery, Juntendo University, Tokyo, Japan

⁸Department of Neurosurgery, Nara Medical University, Kashihara, Japan

⁹Graduate School of Informatics, Kyoto University, Kyoto, Japan

Abstract

Neural representations of visual perception are affected by mental imagery and attention. Although attention is known to modulate neural representations, it is unknown how imagery changes neural representations when imagined and perceived images semantically conflict. We hypothesized that imagining an image would

activate a neural representation during its perception even while watching a conflicting image. To test this hypothesis, we developed a closed-loop system to show images inferred from electrocorticograms using a visual semantic space. The successful control of the feedback images demonstrated that the semantic vector inferred from electrocorticograms became closer to the vector of the imagined category, even while watching images from different categories. Moreover, modulation of the inferred vectors by mental imagery depended on both the image category and time from the initiation of imagery. The closed-loop control of the semantic vectors revealed an asymmetrical interaction between visual perception and imagery.

Introduction

Neural activities in the visual cortex reflect both externally driven “bottom-up” sensory information and internally generated “top-down” signals, such as mental imagery^{1,2} and attention³. Neural decoding using machine-learning techniques has revealed relations between top-down signals and bottom-up information by evaluating their neural representations in the visual cortex. Perceived images can be inferred (decoded) from visual cortical activities as reconstructed images⁴⁻⁶ or semantic attributes of the images^{7,8}. A trained decoder for the perceived images can successfully infer mental imagery content^{5,9}, establishing that perception and imagery have common neural representations in the early⁹ and higher^{5,10,11} visual cortices. Similarly, attention can be inferred by the decoder for perceived images¹². These results suggest that there are common neural representations for both externally driven bottom-up sensory information and internally generated top-down signals of mental imagery and attention.

However, little is known about how the bottom-up information and the top-down signals related to mental imagery interact with each other with regard to neural representations. Previous studies revealed that attention modulates neural representations³ on the basis of semantic similarity to the category of the attended object¹³. In addition, behavioral studies have suggested that imagery acts like weak perception in facilitating subsequent perception^{14,15}. However, it is not known how the neural representations of perceiving images are modulated by imagery when they semantically conflict with each other. For example, when people imagine a human face while watching a landscape such as a mountain view, it remains unclear how the resulting neural representations differ from the neural representations while watching

the same landscape without imagining something (e.g., a human face). Here, we hypothesized that imagining an image would activate a neural representation of perceiving the imagined image even while watching a conflicting image. We evaluated how neural representations resulting from watching an image in category (A) become closer to those in a different category (B) by imagining an image in category (B).

To compare the neural representations while perceiving and imagining various categories of images, we applied neural decoding to electrocorticograms (ECoGs). ECoGs are characterized by high temporal resolution and wide coverage of the cortices¹⁶; these characteristics make ECoGs suitable for evaluating visual information that is sparsely represented in the visual cortex⁷. Moreover, ECoGs have been used to infer several semantic categories of visual stimuli¹⁷⁻¹⁹. In this study, neural decoding was combined with a visual semantic space in which the semantic attributes of an image were embedded into a vector representation⁷; therefore, the changes in neural representations were evaluated as changes in semantic vectors.

Moreover, to explore the effects of imagery on neural representations while perceiving and imagining different images from various categories, we developed a closed-loop system in which the subject was presented images that corresponded to semantic vectors inferred from real-time neural activities (Fig. 1). The semantic vector was inferred by a decoder trained on neural activities when the subject watched images from various semantic categories. Accordingly, if a subject views a feedback image of a certain category without any imagery or attention, images of the same category will be displayed in the closed-loop system. In contrast, if our hypothesis is

true for a certain category, imagining an image from that category would make the semantic vector inferred from the neural activities closer to the semantic vector of the imagined category while watching images from different categories, resulting in the display of an image closer to the imagined category. Even if the change in the semantic vector due to the imagery is small, successive changes in the semantic vectors in the same direction will eventually show the image representing the imagined category. We refer to this intentional control of the semantic vector represented by a feedback image as representational brain-computer interaction (rBCI), in which the feedback images are embedded in a representational space and controlled through the interaction between the decoding-based visual feedback and the top-down intention to alter the feedback. Using the rBCI, we evaluated how neural representations are modulated by imagery in the presence of various types of conflicting bottom-up sensory information.

In this study, we demonstrated that subjects can control feedback images from an rBCI using ECoGs of the visual cortical areas by intending to show images related to specific semantic categories. Moreover, for categories in which the subjects successfully controlled the feedback image, we also demonstrated that the ECoGs during perception of a particular category are modulated by the imagery associated with a different category, resulting in a semantic vector inferred from the ECoGs that was closer to the imagined category.

Results

ECoG recordings and experimental procedure

ECoGs were recorded from 21 subjects with epilepsy (E01–E21) who had subdural electrodes implanted on their occipital or temporal lobes, including the ventral visual cortex (Fig. 2a and Supplementary Fig. 2a; also see Supplementary Fig. 1 and Supplementary Table 1). Among them, 17 subjects (E01–E17) watched six 10-min videos (training videos) consisting of short movies with various semantic attributes (video-watching task). In addition, 12 of these subjects (E01, E03, E06, E07, and E09–E16) watched a 10-min video (validation video) consisting of four repetitions of a 2.5-min movie that was different from the movies in the training video. Based on ECoGs obtained while subjects watched the training video, we constructed a decoder to infer the semantic attributes of the presented scenes. Then, for four subjects (E01–E04), we applied the decoder in a closed-loop condition to present images that were selected based on the semantic attributes inferred from the ECoGs (Fig. 1). Last, for 13 subjects (E01–E09 and E18–E21), we recorded ECoGs while the subjects watched images from a particular category with and without imagery associated with a different category.

High- γ features of ECoGs respond to semantic attributes of movies

Initially, the ECoG frequency bands that consistently responded to the videos were evaluated by the replicability of their power. Power in four frequency bands (α , 8–13 Hz; β , 13–30 Hz; low γ , 30–80 Hz; high γ , 80–150 Hz) was calculated for non-overlapping 1,000-ms time windows from the ECoGs while subjects watched the validation video and were compared across the repeated movies by Pearson's correlation coefficients. Among the four frequency bands, power in the high- γ band responded most consistently to the video stimuli in the early visual area (V1–V4) and the higher visual area (middle temporal complex and neighboring visual areas, ventral

stream visual cortex, medial temporal cortex, and lateral temporal cortex) (Fig. 2b; for consistency depending on the time window, see Supplementary Fig. 2b).

Semantic attributes of each scene in the videos were embedded into a 1,000-dimensional visual semantic space to reveal how the normalized high- γ powers (features) responded to the semantic attributes of the videos. First, the training videos were converted into still images at one-second intervals (3,600 images) and annotated by cloud workers. Then, the annotation of each scene was converted into a 1,000-dimensional vector in the space learned by a word-embedding model called the skip-gram model²⁰ ($V_{true} := \{v_{true}^i \mid i = 1, \dots, 3600 \text{ (scene)}\}$; see Methods and Supplementary Fig. 2c; also see Supplementary Fig. 2d for the consistency of the semantic vectors across annotators). When we applied principal component analysis (PCA) to the proposed semantic vectors of the training videos (V_{true}), the first and second principal components contrasted “human face” scenes from other scenes and “landscape” scenes from “word” scenes, respectively (Fig. 2c, Supplementary Fig. 2e, f, and Supplementary Table 2). To clarify the distribution of scenes in the first and second principal components, we selected 50 scenes with the highest Pearson’s correlation coefficient among the 1,000 values of v_{true}^i and $v_{category}$ ($R(v_{category}, v_{true}^i)$)

($v_{category} : v_{word}, v_{landscape}, \text{ or } v_{face}$; the semantic vector of the word “word”, “landscape”, or average of the semantic vectors of “human” and “face”) from the 3,600 scenes of the training video. The selected 50 scenes in each category were separately distributed in the first and second principal components of the semantic vectors (Fig. 2c; also see Supplementary Fig. 2g). V_{true} successfully captured these semantic attributes of the presented videos.

The high- γ features during the presentation of the selected scenes were compared to elucidate cortical regions that differentially responded to the categories. The high- γ features were calculated from the 1,000-ms ECoGs centered at the time when the annotated image of the selected scenes was presented. The high- γ features in the higher and early visual areas significantly differed depending on the categories ($P < 0.05$, $n = 50$ for each group, uncorrected one-way analysis of variance [ANOVA]; Fig. 2d). The high- γ features in the visual areas differentially responded to the semantic categories.

To evaluate how the high- γ features responded to the semantic attributes while excluding the contribution of these low-level features such as contrast and sounds, we inferred the high- γ features from each electrode based on the semantic features (semantic vectors) and low-level visual and auditory features from the training videos using ridge regression with a 10-fold nested cross-validation. By applying motion energy filters^{8,21} to the videos and modulation-transfer function models²² to the sound of the videos, 2,139 low-level visual features and 2,000 low-level auditory features were acquired for each scene in the training video (see Methods). The high- γ features from the visual areas were significantly explained by semantic features and low-level visual and auditory features (Fig. 2e). Even when the regression weights for the low-level visual and auditory features were set to zero, the high- γ features in the visual areas were still significantly explained by the semantic features ($P < 0.05$, $n = 3,600$ for each electrode, uncorrected one-sided Pearson's correlation test; Fig. 2e), suggesting that the high- γ features in these visual areas responded not only to the low-

level visual and auditory features of the training videos but also to the semantic attributes of the videos that were represented by the semantic vectors.

Decoding of semantic vectors corresponding to the presented scenes

The semantic vector for the i -th scene (v_{true}^i) was inferred from the high- γ features using ridge regression with 10-fold nested cross-validation. The scenes for training and testing in the cross-validation were selected from different movie sources (see Methods and Supplementary Fig. 3a). The accuracy of inferring the semantic vector was evaluated for each principal component of V_{true} . The inferred semantic vectors ($V_{inferred} := \{v_{inferred}^i \mid i = 1, \dots, 3600 \text{ (scene)}\}$) were projected to the k -th direction vector of the PCA ($k = 1, \dots, 1000$) so that the Pearson's correlation coefficient between the projected values and the k -th principal component of V_{true} were calculated for the 3,600 scenes to obtain the projected correlation coefficient ($PrjR^k(V_{inferred}, V_{true})$). For 14 principal components, $PrjR^k(V_{inferred}, V_{true})$ showed a significant positive correlation (Fig. 3a and Supplementary Fig. 3b–d). It should be noted that $PrjR^k(V_{inferred}, V_{true})$ was especially high for the first several principal components.

In addition, for the previously selected 50 scenes from the three categories, we evaluated the accuracy of classifying the category of the presented scene from the inferred semantic vector. For each semantic vector inferred from the high- γ features from all implanted electrodes ($v_{inferred}^i$), Pearson's correlation coefficients with the semantic vectors of the categories were calculated ($R(v_{category}, v_{inferred}^i)$, where $v_{category}$ was v_{word} , $v_{landscape}$, or v_{face}). The classification was considered to be correct when the

$R(v_{category}, v_{inferred}^i)$ was the highest for the category of the presented scene. The accuracies to classify two of the three categories (binary accuracies) were $67.5 \pm 4.7\%$ (mean \pm 95% confidence intervals [CIs] among subjects) for word versus landscape, $70.8 \pm 4.8\%$ for landscape versus human face, and $73.1 \pm 4.5\%$ for human face versus word, all of which were significantly higher than chance level (50%) ($P < 1.0 \times 10^{-6}$, $n = 17$, one-sided one-sample t -test with Bonferroni-adjusted α -level of 0.0167 [0.05/3]; for accuracy in the higher and early visual areas, see Fig. 3b). The accuracy across the three categories was $56.2 \pm 5.6\%$ (also see Supplementary Fig. 3e–g). The three categories of the presented scenes were successfully classified by the high- γ features.

Control of inferred images in the closed-loop condition

Four subjects (E01–E04) participated in a real-time feedback task to control the rBCI using the online decoder that was trained with the high- γ features for all 3,600 scenes of the training videos (Fig. 1 and Fig. 4a, b; also see Supplementary Fig. 4a–d for the accuracy and consistency in the validation video using the online decoder). Prior to this task, the subjects were first informed that images would be presented based on their real-time brain activity, and they were instructed to display a feedback image representing a particular category (i.e., word, landscape, or human face) by visually imagining it. In particular, they were asked to maintain displaying images related to the particular category as long as possible. It is worth noting that subjects were instructed to freely imagine images that they felt well represented the particular category; that is, we did not specify images to be imagined. At the beginning of each trial, a black screen was displayed, and one of the categories (**target category**) was given orally in Japanese (Fig. 4a). High- γ features of 1,000-ms ECoGs were calculated to infer the semantic vector in real-time (online vector: v_{online}) with the

online decoder. The feedback image was selected based on the highest $R(v_{online}, v_{true}^i)$ in the 1,000-dimensional semantic space.

Figure 5a shows a representative result for three consecutive trials in the task. The accuracy of the online control was evaluated as a three-choice task based on the

Fisher z-transformed correlation coefficient between v_{online} and v_{target}

($z(R(v_{online}, v_{target}))$); v_{target} : semantic vector of the target category, v_{word} , $v_{landscape}$, or v_{face}). When we defined a successful trial as that in which frame-averaged

$\overline{z(R(v_{online}, v_{target}))}$ was larger than the other two $\overline{z(R(v_{online}, v_{nontarget}))}$

($v_{nontarget} \in \{v_{landscape}, v_{word}, v_{face}\} \setminus \{v_{target}\}$), the trials with target categories of word and

landscape in Figure 5a were successful. Overall, E01 succeeded in following

instructions with a three-choice accuracy of 45.83%, which was significantly greater than chance ($P = 0.0021$, one-sided permutation test; word vs. landscape, 70.00%;

landscape vs. human face, 61.25%; human face vs. word, 58.75%). For the other three subjects, the accuracies were also significant (E02: 50.00%, $P < 0.0001$; word vs.

landscape, 55.00%; landscape vs. human face, 73.75%; human face vs. word, 72.50%;

E03: 41.67%, $P = 0.031$; word vs. landscape, 62.50%; landscape vs. human face,

46.25%; human face vs. word, 58.75%; E04: 41.67%, $P = 0.0065$; word vs. landscape,

60.00%; landscape vs. human face, 52.50%; human face vs. word, 60.00%).

Therefore, all four subjects succeeded in controlling the inferred semantic vector to be closer to the instructed category.

During the real-time feedback task, E01 succeeded in increasing $z(R(v_{online}, v_{target}))$ more than other two $z(R(v_{online}, v_{nontarget}))$ under the target category of word and landscape (Fig. 5b), resulting in the three-choice accuracy at each frame increasing up to 52.5% in the middle of the trials (Fig. 5c, Supplementary Fig. 5 and Supplementary Table 3). Along with this increase in accuracy, the high- γ power from electrodes in the higher visual area differed depending on the instructions (Fig. 5d), and these differences were associated with high one-way ANOVA F -values (Fig. 5e). When the maximum F -values among the frames were mapped to the cortical surface for all four subjects (Fig. 5f), high F -values were observed around the visual areas. These findings suggested that at least some portion of these electrodes with high F -values contributed to the control of the online vectors and made them closer to the semantic vector of the target category through changes in high- γ power in this closed-loop condition.

The accuracy to control the online vector was also evaluated in the 1,000-dimensional semantic space. The projected correlation coefficients between the online vector and the semantic vector of the target category ($\overline{z(PrjR^k(V_{online}, V_{target}))}$) were positively significant for four principal components (#1, #2, #10 and #15) ($P < 0.05$, $n = 4$, two-sided permutation test with Bonferroni-adjusted α -level of 3.6×10^{-3} [$0.05/14$]; Fig. 5g). The online vectors were successfully controlled along several dimensions in the semantic space in this closed-loop condition.

Modulation of inferred vectors by mental imagery

To evaluate the degree to which the inferred semantic vectors could be modulated by mental imagery, an imagery task was performed by 13 subjects (E01–E09 and E18–

E21) to compare the ECoGs while watching an image with or without imagining an image from a different category. We selected five images representing “word” and five images representing “landscape” that had high $R(v_{true}^i, v_{word})$ and $R(v_{true}^i, v_{landscape})$, respectively, and did not have content relating to another meaning (Supplementary Fig. 6a). In each trial, the subject was first presented an image of a word or landscape for 2 s to memorize (i.e., non-imagery period) and was then presented an image from a different category for another 2 s (i.e., imagery period); during the imagery period, the subject was instructed to visually imagine the first image while watching the second image (Fig. 6a).

The high- γ powers while watching the images from one category were altered by imagining an image from another category. Figure 6b shows a representative time-frequency map of an electrode implanted at V1 in E05. Powers in the high- γ band increased approximately 100–1,000 ms after the presentation of images representing “word” and “landscape” without any imagery; however, when imagining an image from another category, power in the same high- γ frequency band decreased, although the subjects were watching the same image. Similarly, decreases in power in the high- γ band were observed in the early visual area across the 13 subjects (Fig. 6c). The imagery altered power in the high- γ band although the same images were being watched.

For the nine subjects who participated in both the video-watching task and the imagery task (E01–E09), a semantic vector ($v_{inferred}$) was inferred using the high- γ features of the subdural electrodes from 0 to 1 s after the presentation of each image.

Figure 7a shows the $R(v_{inferred}, v_{word})$ and $R(v_{inferred}, v_{landscape})$ for each image presented to E01. In the non-imagery period, each category of images was distributed separately so that two categories of images were classified with areas under the curves (AUCs) of 0.9248 and 0.7936 from the receiver operating characteristic curves of $R(v_{inferred}, v_{word})$ and $R(v_{inferred}, v_{landscape})$, respectively (binary accuracy between the two categories: 80.00%); however, in the imagery period, the distribution of the landscape image moved toward the word image. In fact, the $z(R(v_{inferred}, v_{word}))$ while imagining word images and watching a landscape image significantly increased compared to that while watching a landscape image without the imagery ($\Delta Z_{word} = 0.1570$, $P = 0.0006$, $t(47.81) = 3.44$, $n = 25$ for each group, uncorrected one-sided Welch's t -test; Supplementary Fig. 6b); in contrast, the $z(R(v_{inferred}, v_{landscape}))$ while imagining landscape images and watching a word image was not significantly increased compared to that while watching a word image without the imagery ($\Delta Z_{landscape} = -0.0040$, $P = 0.57$, $t(47.10) = -0.17$).

Among all nine subjects included in this analysis, the inferred semantic vectors were modulated in the direction of the semantic vectors of “word” and “landscape” by imagery. Initially, $R(v_{inferred}, v_{word})$ and $R(v_{inferred}, v_{landscape})$ successfully classified the images of words and landscapes during the non-imagery period using the high- γ features of the subdural electrodes from 0 to 2.0 s (Fig. 7b; binary accuracy between the two categories for 0–1.0 s: $80.8 \pm 9.0\%$ [mean \pm 95% CIs among subjects]). The $z(R(v_{inferred}, v_{word}))$ with the landscape image significantly increased while imagining word images using the high- γ features from 0 to 1.0 s and 1.0 to 2.0 s ($n = 9$, one-sided one-sample t -test with Bonferroni-adjusted α -level of 0.0083 [0.05/6]; Fig. 7c).

Similarly, the $z(R(v_{inferred}, v_{landscape}))$ with the word image significantly increased while imagining landscape images using the high- γ features from 0.5 to 1.5 s (Fig. 7c; for other frequency bands, see Supplementary Fig. 6c, d). In addition, although the accuracies to classify the images of “word” and “landscape” showed a tendency to be higher with the early visual area than with the higher visual area (Fig. 7d), the modulations using the high- γ features from the higher visual area showed a tendency to be higher than those from the early visual area (Fig. 7e). Similar to the modulations using the high- γ features of all subdural electrodes (Fig. 7c), ΔZ_{word} increased immediately after image presentation (0–1.0 s), whereas $\Delta Z_{landscape}$ increased at 1 s after image presentation (0.5–1.5 s) using the high- γ features from the higher visual area. Therefore, it was demonstrated that the modulation of the semantic vector depends on time from the initiation of imagery, the imagined category and/or the category of the presented image. Moreover, different anatomical areas were suggested to contribute to the modulations.

Discussion

This study tested the hypothesis that imagining an image from one category while watching a conflicting image from another category results in neural representations closer to those obtained while watching the image of the imagined category. Using rBCI with real-time visual feedback based on the visual semantic vector inferred from the high- γ features, the subjects succeeded in controlling the inferred semantic vector to move closer to the semantic vector associated with the instructed category. The rBCI enabled an exploratory search for the semantic category for which the hypothesis stood, because the successful control of the feedback image required that the semantic vector inferred from the neural activities becomes closer to the semantic

vector corresponding to the imagined category while feedback images from the various categories were presented to the subject. Then, for the semantic categories successfully controlled in the closed-loop condition with rBCI, modulation of the semantic vector by imagery was evaluated in the imagery task. The imagery task revealed that the inferred vector was modulated such that it moved significantly closer to the imagined category even when watching an image from a different category, although this modulation depended on the particular image category and time from the initiation of imagery. Therefore, these results supported our hypothesis, at least regarding the imagery associated with words and landscapes.

In this study, we developed the rBCI as a novel tool to explore the relationship between top-down signals such as attention and imagery and external stimuli providing bottom-up information. Although previous studies have shown that neural representations can be intentionally modulated by attention and activated by mental imagery, it was unknown whether people could voluntarily control the various images inferred from their neural activity by these top-down intentions, even when watching images from various categories. A previous study demonstrated that people can intentionally control the superposition of two images of familiar individuals by mental imagery and attention based on hippocampal signals in a closed-loop condition²³. However, the feedback image in that study presented no conflict between the visual perception and top-down intention to control the image because the feedback image was the overlapped image of two images that originated from the same category (familiar individual). In addition, some recent studies have demonstrated that people can control the output of a decoder that infers particular features of visual perception (e.g., orientation and color) based on visual cortical activities in a closed-loop

condition²⁴; however, the subjects were not aware of the inferred visual feature during the control. To the best of our knowledge, the present study is the first report showing that people can intentionally control the images inferred from the visual areas in a closed-loop condition by top-down intentions that conflict with the bottom-up sensory information.

The closed-loop condition may improve the accuracy of inferring the imagined category compared to the open-loop condition. A previous study demonstrated that a decoder to infer perceived visual stimuli can identify some objects imagined by eyes-closed subjects; however, the accuracy to identify the imagined objects was low compared to the accuracy to identify the perceived objects¹⁰. Consistent with this result of the previous study, the accuracy to infer the imagined category was low without feedback, which was reflected in the accuracy at the beginning of the trials (Fig. 5c and Supplementary Fig. 5a) when the subject imagined images based on the instruction but the feedback screen was black. In contrast, as the feedback continued, the subjects succeeded in controlling the online vector to be closer to the instructed semantic vectors with higher accuracy. Therefore, the data suggested that the closed-loop condition improved the accuracy of inferring the imagined category compared to the decoding of the imagined category in an open-loop condition.

Mental imagery^{1,2} and attention³ are possible top-down mechanisms by which the inferred images in the rBCI were controlled. In fact, during the real-time feedback control, the subjects tended to focus their attention on specific parts of the feedback image that were close to the instructed category (e.g., subtitles in the images when the word instruction was given), although we instructed them to imagine the instructed

category. However, it is difficult to explain feedback control only by attention. Among the 2,926 images used for the feedback, the human face was a common attribute. In fact, 1,691 images (57.8%) contained the human face attribute; nevertheless, it was difficult to display the images of the human face as instructed. Moreover, in the imagery task, although there were no images that contained both meanings, the neural representation was modulated by the visual imagery, and the inferred vector was altered toward the imagined meaning. These results suggested that real-time feedback was controlled by both attention and mental imagery, which modulated the information inferred from the visual areas.

The imagery task revealed that the modulation was asymmetrical between word and landscape; ΔZ_{word} was the largest in the early time period of the imagery, whereas $\Delta Z_{landscape}$ became significant at 1 s after initiation of the imagery, indicating the modulation depending on the semantic attributes and the time from the initiation of the imagery. Although a previous study demonstrated similar results with word imagery using representational similarity between memorization of words and the recall of memorized words²⁵, the dependency of such modulations on different semantic attributes had not been revealed. Our results demonstrated the asymmetrical interaction of perception and imagery based on its semantic attributes and timing. In addition, the modulation might depend on the anatomical locations of the implanted electrodes. The modulations of the semantic vector (ΔZ_{word} and $\Delta Z_{landscape}$) using the high- γ features from the higher visual area tended to be larger than those from the early visual area. These results are consistent with a previous study showing that higher visual areas in the ventral stream more similarly represent imagery and perception than those in early visual areas¹⁵. It might be easier to alter the activity in

the higher visual areas to be closer to the imagined category because semantic information of the perception and imagery are represented similarly in higher visual areas¹⁵. Further studies are necessary to reveal how the bottom-up information represented by cortical activities is modulated by top-down signals by different combinations of the image categories and by anatomical location.

This study was characterized by the use of semantic space to test the hypothesis. To extract the semantic attributes of the images, we constructed the semantic space based on the skip-gram model using annotations by humans, which were consistent across annotators (Supplementary Fig. 2d), and confirmed that the semantic vectors of the images represented the semantic attributes of images such as word, landscape, and human face (Fig. 2c). Moreover, it was shown that the high- γ features in the visual areas while watching the training videos were significantly inferred from the semantic vectors even when excluding the contribution of the low-level visual and auditory features (Fig. 2e). These results demonstrated that the semantic vectors used in this study contained the “semantic” information of visual stimuli and succeeded in explaining the visual cortical responses while watching videos containing various semantic attributes. It is also worth mentioning that these results were consistent with some previous studies demonstrating that the semantic attributes of visual stimuli were represented in the ECoGs from the visual areas^{19, 26, 27}. Compared to these studies, the present study employed a large number of subjects and various visual stimuli to reveal semantic representations in the ECoGs; in addition, with the decoding analysis, it was shown that the ECoGs from visual areas are informative for inferring the semantic vectors of the presented images (Fig. 3a, b). Therefore, it was

concluded that the semantic attributes of the images were inferred from the high- γ features from visual areas.

It remains unknown how semantic space affects the controllability of the rBCI. Semantic space can be based on semantic categories by human judgment²⁸⁻³⁰ or automatically learned from a large text corpus by language models^{20, 31}. Interestingly, both methods extract similar spaces³². Moreover, recent studies have demonstrated that intermediate layers of deep neural networks are applicable for decoding visual stimuli⁵. It should not be forgotten that the best space for decoding might differ from that for the control of rBCI. In our results, the decoding accuracy in the open-loop condition was higher for the first principal component than for the second principal component (Fig. 3a). On the other hand, the decoding accuracy in the closed-loop condition was higher for the second principal component than for the first principal component (Fig. 5g). The controllability of the inferred image did not seem to depend on the decoding accuracy in the open-loop condition but might depend on the semantic attributes. This result seems consistent with previous studies suggesting that the high accuracy of identifying perceived images by perception decoders does not guarantee high accuracy in identifying mental imagery by the decoder^{33, 34}. Because a direction along which decoding is easy in perceived images does not always mean that subjects can voluntarily modulate neural activity in that direction by imagery, the optimum space with the best controllability for the rBCI should be investigated in further studies under closed-loop conditions.

Last, rBCI might be useful as a communication device for severely paralyzed patients, such as those with amyotrophic lateral sclerosis (ALS)³⁵, to display patients' thoughts

as images. For these individuals, a brain-computer interface (BCI)³⁶ is in high demand³⁷ and succeeds in expressing their thoughts by controlling some communication tools^{16, 38-40}, although most BCIs rely on motor-related activities, which degenerate in patients with ALS. Because visual cortical activity persists for a long time⁴¹ even in patients with ALS, rBCI using visual cortical activity might be used as a stable communication device for patients with severe ALS⁴². Further study of rBCI will allow the development of novel communication devices for severely paralyzed patients.

Materials and Methods

Subjects

This study included a total of 21 subjects with drug-resistant epilepsy (14 males; 25.0 ± 11.2 years old, mean \pm standard deviation [SD] on the day of the experiment) from three sites (Osaka University Medical Hospital, Osaka, Japan; Juntendo University Hospital, Tokyo, Japan; Nara Medical University Hospital, Nara, Japan). One subject participated twice because of a second surgery after an interval of 2 years (E07 and E11). The subjects were implanted with intracranial electrodes prior to the study for the purpose of treating their epilepsy (number of subdural electrodes: 64.4 ± 17.0 ; number of depth electrodes: 10.8 ± 10.0). Prior to the experiment, written consent was obtained from all subjects after explaining the nature and possible consequences of the study. The experiment was performed in accordance with the experimental protocol approved by the ethics committee of each hospital (Osaka University Medical Hospital: Approval No. 14353, UMIN000017900; Juntendo University Hospital: Approval No. 18-164; Nara Medical University Hospital: Approval No. 2098).

Experimental settings and ECoG recordings

The subjects either sat on beds in their hospital rooms or were seated on chairs to perform the experimental tasks. A computer screen was placed in front of the subjects to show the video stimuli, the real-time feedback image, or stimuli for the imagery task. During the experiment, ECoGs were recorded at 10 kHz by EEG-1200 (Nihon Koden, Tokyo, Japan) by referencing the average of two intracranial electrodes. The presentation timing of the visual stimuli and real-time feedback images was monitored by DATAPixx3 (VPixx Technologies, Quebec, Canada) such that the digital pulse at

the timing of the presentation was recorded synchronously with the ECoG. Gaze data were also recorded using an eye-tracking system (Tobii, Danderyd, Sweden) to monitor if the subjects were performing tasks, with the exception of those who wore glasses for vision correction or those in whom the position of wirings to the intracranial electrodes interfered with the system.

Experimental procedures

Seventeen subjects (E01–E17) participated in the **video-watching task** to evaluate the relationship between the semantic vector of each scene and ECoGs while watching the scenes. Four subjects (E01–E04) participated in the **real-time feedback task**, in which a decoder trained with ECoGs recorded during the video-watching task was used to determine feedback images. Moreover, 13 subjects (E01–E09 and E018–E21), including the 4 subjects from the real-time feedback task, participated in the **imagery task** to elucidate modulation of inferred semantic vectors (output of the decoders) by visual mental imagery.

Video-watching task

Task procedures

While ECoGs were recorded, seventeen subjects (E01–E17) watched the six 10-min videos (training videos). Among them, 12 subjects (E01, E03, E06, E07, and E09–E16) watched a 10-min video (validation video) composed of four repetitions of a 2.5-min movie. ECoGs of baseline brain activity were recorded prior to presentation of each video using one of the following two methods. (1) Thirteen subjects (E05–E17) were instructed not to think of anything or move and to remain calm for 30 s (**resting without images**). (2) The remaining four subjects (E01–E04) were presented with

sixty images for 1 s each and subsequently participated in the real-time feedback task; the subjects were instructed to watch the images by keeping their eyes on the red fixation point at the center of the images without thinking of anything or moving while remaining calm (**resting with 60 images**). The images were selected from ImageNet⁴³ and cropped at their center to create square images; the order of the images was randomized for each video. In addition, ECoGs were recorded during a 30-s resting period (which is the same condition as in method 1).

Immediately after recording the baseline brain activity, one of the 10-min videos was presented to the subject with audio of the video played from a pair of speakers. No fixation point was presented during the video, and the subjects were instructed to watch the video freely. To minimize the subject's fatigue, some interval was taken between the presentations of the six training videos; consequently, the entire task for the training videos took 1 to 3 days to complete. The validation video was presented after the presentation of training videos.

Videos for visual stimuli

We created the training videos and the validation video composed of 224 and 44 short cinema or animation clips, respectively, each of which was cut out from one of 75 trailers or behind-the-scenes features downloaded from Vimeo. Those trailer or behind-the-scene features originated from 70 video sources (cinema or animation). The median duration of the clips was 16 s (interquartile range, 14 to 18 s), and they were sequentially concatenated to create six 10-min videos as training videos and a 2.5-min video to be repeated four times, resulting in a 10-min validation video. The videos contained scenes that varied widely in semantic content, such as scenery of

nature, space, animals, food, people and text. No overlapping scenes were included in the videos except the repetitions in the validation video; it should be noted that the training videos and the validation videos did not have any overlap although they originated from the same trailers or behind-the-scenes features.

Construction of the skip-gram model

A skip-gram model was trained using the Japanese Wikipedia dump data following the procedure described in a study by Nishida and Nishimoto⁷. The Japanese text of the articles in the Wikipedia dump was segmented into words and lemmatized to create a text corpus. This conversion was performed using MeCab⁴⁴, an open-source text segmentation software, and the Nara Institute of Science and Technology (NAIST) Japanese dictionary, a vocabulary database for MeCab. Words other than nouns, verbs, and adjectives were discarded from the text corpus, in addition to those that appeared fewer than 120 times. After these pre-processing steps, the text corpus had 365,312,470 words, including 94,337 nouns, 4,922 verbs, and 631 adjectives. A skip-gram model was trained with the text corpus using the Gensim Python library with the following parameters: dimension of word vector representation, 1,000; window size, 5; number of negative samples, 5; use of hierarchical Softmax, no. For presentation in this article, Japanese words (i.e., annotations and the instructions in the real-time feedback task) were translated to English using Google Translate.

Construction of the semantic vector

From the six 10-min training videos and the 2.5-min movie in the validation video, a still image of the video scene was extracted every second (Supplementary Fig. 2c). Each image (scene) was manually annotated by five annotators with descriptive

sentences that had 50 or more Japanese characters. The annotators were native Japanese speakers who were neither authors nor subjects. Semantic vectors for each scene were constructed based on the vector representations learned by the skip-gram model²⁰, which enables linear operation between vectors representing words (e.g., vector operation of “king” – “man” + “woman” results close to “queen”^{45, 46}). All annotations were first segmented into words and lemmatized using MeCab and the NAIST Japanese dictionary. Among the lemmatized words in the annotations, words that did not exist in the text corpus were discarded. Each word was converted into the corresponding 1,000-dimensional vector representation using the trained skip-gram model. Based on the linear relationships between semantic vectors, semantic vectors were constructed by averaging the vector representations of the lemmatized word, first within each annotation, and then across the five annotations for each scene (denoted as $V_{true} := \{v_{true}^i \mid i = 1, \dots, 3600 \text{ (scene)}\}$ for the training videos). It should be noted that the average of the correlation coefficients across vectors for the five annotators for the same scene was 0.7523 ± 0.0013 (mean \pm 95% CIs among the scenes), suggesting the high consistency of the vectors across the annotators.

Evaluation of the visual semantic space

To visualize the space spanned by the semantic vectors, PCA was applied to the 3,600 semantic vectors (V_{true}) from the training videos to reveal their major components. To create the vector representation for “human face” (v_{face}), the vectors for “human” and “face”, which were learned by the skip-gram model, were averaged. For the vector representation for “word” and “landscape”, the corresponding vectors in the skip-gram model (v_{word} and $v_{landscape}$) were used.

Extraction of low-level visual and auditory features

Low-level visual and auditory features were extracted by applying motion energy filters^{8,21} to the training videos and modulation-transfer function models²² to the sound of the training videos, respectively. To extract low-level visual features, the videos were down-sampled in frame rate and in spatial resolution to create videos with 15 fps and 171×96 pixels of RGB colors. The videos were then cropped at their center and converted to Commission Internationale de l'Éclairage L* A* B* color space. Motion energies were acquired from the luminance of the videos by applying spatiotemporal Gabor filters differing in motion direction (0, 45, ..., 315 degrees; orientation of each filter was perpendicular to the motion direction), spatial frequency (0, 1.5, 3, 6, 12, and 24 cycles/image), and temporal frequency (0, 2, and 4 Hz), spatially positioned on a square grid with a distance of 4.0 SDs of the spatial Gaussian envelope. By averaging the log-transformed motion energies within the 1-s time window corresponding to each scene, low-level visual features were calculated as 2,139-dimensional vectors. Meanwhile, the low-level auditory features were extracted from the sound of the videos using modulation-transfer function models⁴⁷. The sound of the videos was converted to a spectrogram using 128 bandpass filters with a window size of 25 ms at a step of 10 ms. By applying 100 modulation-selective filters (10 spectral modulation scales and 10 temporal modulation rates) to the spectrogram, modulation energies were calculated. The modulation energies were then log-transformed and averaged within the 1-s time window corresponding to each scene and within 20 nonoverlapping frequency bands evenly spaced in log-space from 20 Hz to 10 kHz, resulting in 2,000-dimensional vectors of low-level auditory features.

Real-time feedback task

Task procedures

Four subjects (E01–E04) participated in the real-time feedback task that was conducted on a different day from the video-watching task. The subjects were first informed that the images would be presented based on their real-time brain activity and were instructed to control the feedback image on the screen by visual imagery so that the feedback image keeps showing the instructed category (Fig. 1).

The real-time feedback task was composed of four sessions, each consisting of 30 trials. Prior to the first session, ECoGs of the baseline brain activity were recorded while subjects watched the same 60 images that had been presented before the video-watching task (i.e., resting with 60 images). Each image was presented for 1 s in randomized order without intervals. During this period, the subjects were instructed to watch the images by keeping their eyes on the red fixation point at the center of the images without thinking of anything or moving while remaining calm.

On each trial, a black screen was first presented for 4.5 s; 2.5 s after display of the black screen, one of the following three instructions (target categories) whose durations were less than 1.0 s was given orally in Japanese: “Moji” (word), “Fuukei” (landscape), or “Hito-no-kao” (human face). After presentation of the black screen, 32 frames of feedback images were presented, each with a duration of 250 ms (Fig. 4a). The feedback image shown on the screen was one of 2,926 images out of 3,600 annotated images in the training videos. The other 674 images were discarded because they were blurry or otherwise unclear or because they contained text that might evoke negative feelings (e.g., “death”).

Real-time decoding

In the real-time feedback task, ECoGs were acquired and decoded in real time to infer a semantic vector. The ECoGs of the most recent 1 s were re-referenced by pre-processing, converted into raw features, and compensated with the re-referenced baseline ECoGs from the resting with 60 images condition recorded just before the real-time feedback task (for details, see *Signal pre-processing* and *Calculation of high- γ features*; for electrodes used in the real-time decoding, see Fig. 4b). Then, the semantic vector was inferred from the compensated decoding features for the feedback. The feedback image was determined based on the highest Pearson's correlation coefficient between the online vector (v_{online}) and the true semantic vectors of the 2,926 scenes. The first v_{online} , used to determine the first feedback image in each trial, was the inferred vector ($v_{inferred}$) from the 1-s ECoGs during presentation of the black screen. The subsequent v_{online} was calculated as the linear interpolation of the previous online vector (v_{online}^{prev}) and the inferred vector of the most recent 1-s ECoGs, which were acquired at 250-ms intervals with the previous decoding ($v_{online} = \alpha \cdot v_{inferred} + (1 - \alpha) \cdot v_{online}^{prev}$). The interpolation weight (α) was manually adjusted prior to the first real-time feedback session by experimenters and fixed throughout all sessions (E01 and E04, $\alpha = 0.5$; E02, $\alpha = 1.0$; E03, $\alpha = 0.4$). Within each real-time feedback session, each instruction was given 10 times in randomized order, and the sessions were repeated four times for each subject at such an interval that the subject could take a break. The system delay from the acquisition of ECoGs to presentation of the feedback image was 195.2 ± 29.2 ms (mean \pm SD; measured from the real-time sessions with E01).

Imagery task

Task procedure

The subjects visually imagined mental images in one category while watching various images in another category (Fig. 6a). The images shown in this task originated from the 3,600 annotated images of the training videos. We selected five images for both the word and landscape categories based on the highest Pearson's correlation coefficients between the true semantic vector and the semantic vector for word and landscape ($R(v_{true}^i, v_{word})$ and $R(v_{true}^i, v_{landscape})$), although some images were rejected such that no images included meanings related to a different category, and the selected images had a clear meaning of either word or landscape (for selected images, see Supplementary Fig. 6a). At the beginning of the task, baseline ECoGs were acquired for 30 s, during which period the subject was instructed not to think of anything or move and to remain calm (resting without images). Then, on each trial, the first image was presented for 2 s (non-imagery period), and the second image, selected from a different category, was presented for another 2 s (imagery period). No fixation points were shown during the presentation of these images. The intertrial interval was 1 s, and the subject was presented with a black screen with a white cross at its center during this period. For all combinations of images between the two categories, the trials were repeated; hence, the number of trials for one session was 50. The presentation order was randomized. The subjects were instructed to memorize the first image and then to visually imagine the memorized image while watching the second image. Twelve subjects (E01–E08 and E18–E21) participated in the imagery task for one session, whereas E09 participated in two sessions.

Signal pre-processing

Based on visual inspection of the recorded ECoGs in the video-watching task (E01–E17) or in the imagery task (E18–E21), noisy channels were discarded from subsequent analyses. Neither down-sampling nor filtering was performed as signal pre-processing.

Signal pre-processing for the video-watching task and imagery task

ECoGs obtained during the video-watching task and the imagery task were re-referenced by common averaging across the noise-free channels.

Signal pre-processing for real-time feedback task

During the real-time decoding (and for training of the decoder used in the real-time feedback task), a subset of the noise-free channels was used to re-reference the ECoGs to increase performance in the real-time feedback task. (1) We first discarded channels in regions that were considered to not contribute to the control of the inferred vector (e.g., channel whose electrode was located in the frontal lobe). (2) Channels that did not show a stable response to the visual stimuli were discarded as follows: (2-1) ECoGs from the video-watching task were re-referenced using common averaging across the remaining channels. (2-2) From the re-referenced signals, raw features during the presentation of the images in the resting with 60 images condition were calculated to discard channels that satisfied the following criteria in at least one video: $standard\ deviation(feature_i^{baseline,raw} / feature_i^{baseline0,raw}) > 0.5$ (see *Calculation of high- γ features*). (2-3) The ECoGs in the video-watching task were again re-referenced using common averaging across the remaining channels to train the decoder. Re-referencing using the same subset of the noise-free channels was

performed during the real-time decoding and in the analysis of the ECoGs recorded in the real-time feedback task (for locations of selected electrodes, see Fig. 4b).

Calculation of powers for consistency analysis

For the consistency analysis, powers were calculated from 1-s ECoGs of a channel ($X_{signal}(t)$) while the subjects were watching the validation video. Using a Hamming window and fast Fourier transformation (FFT), the power spectrum density was calculated ($PSD_f(X_{signal}(t)) [uV^2 / Hz], f : frequency [Hz]$) to be averaged within the α (8–13 Hz), β (13–30 Hz), low- γ (30–80 Hz), and high- γ (80–150 Hz) frequency bands.

Calculation of high- γ features

From 1-s ECoGs of a channel ($X_{signal}(t)$) and the corresponding baseline signals from the same channel ($X_{baseline}(t)$), decoding features were calculated. The power spectrum density of the signal was calculated using a Hamming window and FFT; the power spectrum density was then averaged across the high- γ frequency band to calculate the raw features as follows:

$$feature^{signal,raw} := \left(\frac{1}{|\{f \in [80, 150]\}|} \sum_{f \in [80, 150]} PSD_f(X_{signal}(t)) \right)^{0.5} [uV / Hz^{0.5}].$$

To compensate for impedance changes for each intracranial electrode from the condition during the first training video presentation in the video-watching task, we evaluated the compensation factor ($comp$) to calculate decoding features ($feature^{signal} = feature^{signal,raw} / comp$) using one of the following two methods, each of which corresponded to the recording method for the baseline signals.

(1) *Resting without images:*

The ECoGs during the 30-s resting baseline ($X_{baseline}(t)$) were divided into 30 time windows of 1 s each. For each time window, the raw feature ($feature_i^{baseline,raw}$, $i=1,\dots,30$ (time window)) was calculated. The same procedure was applied to the ECoGs during the 30-s resting baseline recorded just before presentation of the first training video ($X_{baseline0}(t)$) to acquire raw features ($feature_i^{baseline0,raw}$). The compensation factor was defined as follows:

$$comp := \sum_i feature_i^{baseline,raw} / \sum_i feature_i^{baseline0,raw} .$$

(2) *Resting with 60 images:*

The ECoGs from 0 to 1 s after the presentation of each of the 60 images were extracted from the baseline ECoGs ($X_{baseline}(t)$) to obtain raw features ($feature_i^{baseline,raw}$, $i=1,\dots,60$ (image)). In the same manner, from the ECoGs recorded prior to presentation of the first training video ($X_{baseline0}(t)$), the signals from 0 to 1 s after presentation of the images were extracted and converted to the raw features ($feature_i^{baseline0,raw}$). By paring raw features for the same image, the compensation factor was defined as follows: $comp := \sum_i (feature_i^{baseline,raw} / feature_i^{baseline0,raw}) / 60$.

Construction of the decoder

Throughout this study, ridge regression was used to infer semantic vectors from decoding features. To train a regression model from a dataset that consisted of decoding features and corresponding true semantic vectors, cross-validation⁴⁸ was applied; the decoding features in the training dataset of each fold were standardized by z-scoring using its mean and SD for each dimension of the features. The decoding

features in the testing dataset were standardized using the same means and SDs calculated solely with the training dataset to prevent any data leakage⁴⁹. For each candidate of the regularization parameter of the ridge regression ($10^{-8}, 10^{-7}, \dots, 10^8$), a regression model was trained for each dimension of the visual semantic space to decode the standardized decoding features of the testing dataset. Finally, all decoding features in the entire dataset were again standardized by z -scoring, using the mean and SD for each dimension of the features; a ridge regression model was trained for each dimension of the visual semantic space with the regularization parameter that maximized the average of the dimension-wise correlation coefficients in the visual semantic space ($\overline{\{DimR^k(V_{inferred}, V_{true})\}}$; see *Measure of accuracy for the inferred semantic vectors*) between the sequence of the inferred semantic vector ($V_{inferred} := \{v_{inferred}^i \mid i: \text{scene in entire dataset}\}$) and the true semantic vector ($V_{true} := \{v_{true}^i\}$). When the trained decoder was applied to new decoding features, the new decoding features were standardized by the same means and SDs of the entire dataset before applying the regression models.

Measure of accuracy for the inferred semantic vectors

To evaluate the decoding accuracy of the semantic vectors inferred from the ECoGs, we used the following four measures.

(1) Dimension-wise correlation coefficients ($DimR^k$)

Dimension-wise correlation coefficients were calculated as a Pearson's correlation coefficient between sequences of the true semantic vectors

($V_{true} := \{v_{true}^i \mid i: \text{tested scene}\}$) and the inferred semantic vectors

($V_{inferred} := \{v_{inferred}^i\}$) for each dimension

($\{DimR^k(V_{inferred}, V_{true}) \mid k = 1, \dots, 1000 \text{ (dimension in the visual semantic space)}\}$).

(2) Projected correlation coefficients ($PrjR^k$)

Projected correlation coefficients ($\{PrjR^k(V_{inferred}, V_{true}) \mid k = 1, \dots, 1000\}$) were measured using the direction vectors of the true semantic vectors acquired by PCA for the training videos (see *Evaluation of the visual semantic space*). Each inferred semantic vector from the tested scenes

($V_{inferred} := \{v_{inferred}^i \mid i: \text{tested scene}\}$) was projected to the k -th direction vector of the PCA to calculate Pearson's correlation coefficients between the projected values and the k -th principal component of the corresponding true semantic vectors ($V_{true} := \{v_{true}^i\}$).

(3) Scene-wise correlation coefficient ($R(v_{inferred}^i, v_{true}^i)$)

The scene-wise correlation coefficient was calculated to evaluate the accuracy for each image. The scene-wise correlation coefficient was defined as the Pearson's correlation coefficient between the true and inferred semantic vectors for each scene ($R(v_{inferred}^i, v_{true}^i)$).

(4) Scene-identification accuracy

Scene-identification accuracy indicated the accuracy in identifying the corresponding scene from the inferred semantic vector. For a scene (i) to be tested, the true scene-wise correlation coefficient ($R(v_{inferred}^i, v_{true}^i)$) between the inferred semantic vector ($v_{inferred}^i$) and the true semantic vector (v_{true}^i) was compared in a pairwise manner with other scene-wise correlation coefficients between the inferred semantic vector and true semantic vectors of other scenes to

be compared ($\{v_{true}^j \mid i \neq j, j : \text{scene to be compared}\}$). The proportion of compared scenes with which the inferred semantic vector correlated less than or equal to the true scene-wise correlation coefficient was calculated, and the average of the proportions was defined as the scene-identification accuracy of the tested scene

$$acc^i := \sum_j (C_{i,j}) / |\{j\}| \text{ where } C_{i,j} := 1 \text{ if } R(v_{inferred}^i, v_{true}^i) > R(v_{inferred}^i, v_{true}^j) \text{ otherwise } 0$$

Analysis for video-watching task

Consistency analysis of cortical activity while watching the validation video

Consistency of the cortical activity responding to the movies was evaluated using the four repetitions in the validation video. For each electrode, powers in four frequency bands (α , β , low γ , and high γ) were calculated from 1-s ECoGs obtained without overlap (150 values for each electrode, band, and repetition). For all six possible pairs among the four repetitions, Pearson's correlation coefficients were calculated between the powers; the correlation coefficients were then Fisher z-transformed to be averaged across the pairs.

Extraction of high- γ features

For further encoding and decoding analyses, high- γ features were extracted from pre-processed ECoGs recorded during the video-watching task. For each annotated image in the videos, ECoGs within a time window of ± 500 ms combined with baseline ECoGs recorded prior to each video presentation were used to calculate the features. For the four subjects who participated in the real-time feedback task (E01–E04), the baseline ECoGs from the resting with 60 images condition were used for

compensation to evaluate the decoding performance during the video-watching task in a condition closer to the real-time decoding task; for the other thirteen subjects (E05–E17), baseline ECoGs from the resting without images condition were used for compensation.

Division of scenes for nested cross-validation

Scenes in the training videos were divided into 10 groups without any overlapping scenes between them for further encoding and decoding analyses, both of which were based on regression analyses with 10-fold nested cross-validation. To prevent overestimation of the accuracy that might be caused when similar scenes from the same video source were divided into different groups, the division of the scenes was determined using a generic algorithm such that (1) scenes from the same video source were kept in the same group and (2) the imbalance of the number of scenes in each group was minimal.

Inference of the high- γ features from the semantic vectors and the low-level visual and auditory features (encoding analysis)

For each electrode, the high- γ features while watching the training videos were inferred from the semantic vectors and the low-level visual and auditory features of the videos by using ridge regression. Low-level visual and auditory features were obtained by applying motion energy filters^{8,21} to the training video and modulation-transfer function models²² to the sound of the videos (see *Extraction of low-level visual and auditory features*). The semantic features (semantic vectors) and low-level visual and auditory features were all concatenated to infer high- γ features at each electrode using 10-fold nested cross-validation in the following procedure. Based on

the division of the scenes (see *Division of scenes for nested cross-validation*), the dataset, consisting of the concatenated features and the high- γ features, was divided into 10 smaller datasets. As described in *Construction of the decoder*, for each dataset (test dataset), a regression model was trained using samples from all other datasets (training dataset) to infer the test dataset. In this way, the regularization parameter was selected without any over-fitting⁴⁹. To evaluate the contributions of each feature set (semantic features, low-level visual features, or low-level auditory features), each test dataset was inferred with the regression model whose weights for the other two feature sets were set to zero.

Inference of the semantic vectors from the high- γ features in the open-loop condition (decoding analysis)

Semantic vectors corresponding to all 3,600 scenes of the training videos were inferred from the high- γ features using 10-fold nested cross-validation. The dataset, consisting of the decoding features (high- γ features) and true semantic vectors, was divided into 10 smaller datasets without any overlapping samples between them (see *Division of scenes for nested cross-validation*). For each dataset (test dataset), a decoder was trained using samples from all other datasets (training dataset; see *Construction of the decoder*) to decode the test dataset so that the regularization parameter was selected without any over-fitting⁴⁹. To assess the decoding accuracy in higher and early visual areas, the decoding features from subdural electrodes in each area were decoded with the same procedure.

Evaluation of binary accuracy and accuracy among three categories

Decoding performance in the open-loop condition was evaluated based on the Pearson's correlation coefficients (scene-wise correlation coefficients) of the inferred semantic vector ($v_{inferred}$) with the semantic vectors of the categories ($R(v_{category}, v_{inferred})$), where $v_{category}$ was v_{word} , $v_{landscape}$, or v_{face} (1) for the three categories and (2) for each pair of categories among the three categories (binary accuracy). The classification was considered correct when the $R(v_{category}, v_{inferred})$ was the highest for the category of the presented scene.

Decoder construction and analysis for the real-time feedback task

Construction of a decoder for real-time feedback

The decoder used in the real-time feedback task was trained using the decoding features from all 3,600 scenes of the six training videos presented in the video-watching task with the regularization parameter optimized by the cross-validation (for details, see *Signal pre-processing* and *Construction of the decoder*). The baseline ECoGs recorded in the resting with 60 images condition were used to compensate the decoding features. For the cross-validation used in the decoder training, the decoding features were divided such that those from the same recording day were treated as a group to maximize decoding performance on a different day from the measurement of the training data. Consequently, two-fold cross-validation was applied for E03 and E04. Because E01 watched the training videos in one day, three-fold cross-validation was used to group the scenes as being from the first and second videos, the third and fourth videos, and the fifth and sixth videos. The same three-fold cross-validation was applied for E02, who watched one video on one day and the other five videos on a different day.

Evaluation of real-time feedback task

Performance in the real-time feedback task was evaluated using the online vectors ($v_{online}^{i,j}$ where $i=1,\dots,120$ (trial) and $j=1,\dots,32$ (frame)), based on which the feedback images were selected, by the following three methods.

(1) By considering each trial of the real-time feedback task as a three-choice trial among the three instructions, the prediction accuracy of the target category was evaluated. For each frame in a trial, the Pearson's correlation coefficients of the online vector with the semantic vectors of the three categories ($v_{instruction}$, v_{word} , $v_{landscape}$, and v_{face}) were calculated. Then, the correlation coefficients were Fisher z-transformed and averaged across the 32 frames in the trial

$\overline{(z(R(v_{online}^j, v_{instruction})))} := \sum_j z(R(v_{online}^{j,j}, v_{instruction})) / 32$). If the (Fisher z-transformed

and) frame-averaged correlation coefficient with the semantic vector of the target category (e.g., $\overline{(z(R(v_{online}^j, v_{word})))}$ for target category of word) was higher than the

other two ($\overline{(z(R(v_{online}^j, v_{word})))} > \overline{(z(R(v_{online}^j, v_{landscape})))}$ and

$\overline{(z(R(v_{online}^j, v_{word})))} > \overline{(z(R(v_{online}^j, v_{face})))}$), the prediction on that trial was considered to be correct.

(2) For all pairs of categories among the three categories, the same procedure as (1) was performed using 80 trials whose target categories were the selected categories.

(3) For the directions (acquired as the direction vectors by PCA) along which the semantic vectors were significantly inferred with positive projected correlation coefficients in the open-loop condition, the projected correlation coefficient

($\{PrjR^k(V_{online}, V_{target}) | k : \text{significant direction}\}$) was evaluated between the online

vectors of all frames of all trials concatenated ($V_{online} := \{v_{online}^{i,j}\}$) and the semantic vector of their corresponding target category ($V_{target} := \{v_{target}^{i,j}\}$).

Analysis for the imagery task

Time-frequency decomposition analysis

Time-frequency decomposition was performed on ECoGs in the imagery task. For each subdural electrode, ECoGs were obtained for each image presentation in the non-imagery period and the imagery period, and the `newtimef` function in `eeglab`⁵⁰ with an FFT window size of 8,192 was applied. For cortical mapping of the powers, the time-frequency map of the decomposed powers for each presentation was converted into decibels and averaged within the high- γ frequency band and 0 to 1 s.

Evaluation of modulation of inferred semantic vectors by mental imagery

This analysis was performed for the subjects who participated in both the video-watching task and the imagery task (E01–E09). For each of the first and second images in the imagery task, pre-processed ECoGs from 0 to 1 s after the presentation of images were extracted and converted to decoding features using the pre-processed ECoGs of the 30-s resting baseline (resting without images) recorded just prior to the imagery task as the compensation baseline. Decoding features from the subdural electrodes were decoded using a decoder trained in the same manner as the one used in the real-time decoding with the exception of the use of decoding features from the video-watching task compensated with the 30-s resting ECoGs recorded in the resting without images condition. With the inferred semantic vector ($v_{inferred}$), Pearson's correlation coefficients of the semantic vector for word ($R(v_{inferred}, v_{word})$) and

landscape ($R(v_{inferred}, v_{landscape})$) were calculated. Distinguishability of the category of the presented image was evaluated by AUC based on these correlation coefficients with each semantic vector. The modulation of $R(v_{inferred}, v_{word})$ by imagining word images (ΔZ_{word}) was evaluated as the difference in the Fisher z-transformed and averaged correlation coefficients with the semantic vector for word ($\overline{z(R(v_{inferred}, v_{word}))}$) in the second and first presentations of landscape images (i.e., in the imagery and non-imagery periods, respectively). Similarly, the modulation of $R(v_{inferred}, v_{landscape})$ by imagining landscape images ($\Delta Z_{landscape}$) was evaluated as the difference in the Fisher z-transformed and averaged correlation coefficients with the semantic vector for landscape ($\overline{z(R(v_{inferred}, v_{landscape}))}$) in the second and first presentations of word images. The same procedure above was repeated for ECoGs from 0.5–1.5 s and 1.0–2.0 s after image presentation and for the subdural electrodes in higher and early visual areas.

Evaluation of binary accuracy during the non-imagery period

Binary accuracy to predict the category of the images presented during the non-imagery period was calculated based on the inferred vectors used to evaluate the modulation. For each presentation of an image in a category, the true scene-wise correlation coefficient between the inferred semantic vector from 0–1 s after the image presentation and the true semantic vector of the category was compared with the scene-wise correlation coefficient between the inferred semantic vector and true semantic vectors of another category. The proportion of the images that showed higher correlation coefficients with the semantic vectors of corresponding categories was defined as the binary accuracy.

Localization of intracranial electrodes

The cortical surface of each subject was first extracted from T1-weighted magnetic resonance images using FreeSurfer⁵¹. The positions of the intracranial electrodes were manually located using BioImage Suite⁵² from computed tomography images that were co-registered to the T1-weighted magnetic resonance images. Then, the positions of the subdural electrodes were mapped onto the cortical surface using the intracranial electrode visualization toolbox⁵³. The cortical surface was registered to the surface of a template brain (fsaverage) to locate the positions of each electrode on the normalized brain (Fig. 2a and Supplementary Fig. 1). For the area-based analysis, each subdural electrode was assigned to one of 22 regions based on the parcellation of the human connectome project (vid. supplementary neuroanatomical results)⁵⁴. Moreover, to locate the position of each electrode on the contralateral hemisphere of the template brain, another registration was performed on the template brain that was flipped left to right.

Statistics and Reproducibility

The difference in the high- γ features while watching scenes corresponding to the three categories, each with 50 scenes, was tested with one-way ANOVA (Fig. 2d).

The correlation coefficients between the high- γ features and the inferred features while watching the training videos were tested by one-sided Pearson's correlation test (Fig. 2e). The one-sided test was applied because successful regression results in positive correlation coefficients.

The inferred semantic vectors in the open-loop condition using high- γ features were tested for each principal component of the PCA using a two-sided permutation test (Fig. 3a). The Fisher z-transformed and subject-averaged projected correlation coefficient ($\overline{z(PrjR^k(V_{inferred}, V_{true}))}$) for each principal component was compared to a corresponding chance-level distribution. The chance distributions were created by (1) splitting the true semantic vectors based on the video clips, (2) shuffling their order, (3) concatenating them, and (4) calculating the subject-averaged projected correlation coefficient in exactly the same way. The permutation was performed 1 million times. The α -level was adjusted by Bonferroni correction for the number of components, which was 1,000.

Binary accuracies of all subjects using high- γ features were tested against chance level (50%) using one-sided one-sample t -tests. Because the binary accuracy was expected to be higher than the chance level, a one-sided test was used. The α -level was adjusted by Bonferroni correction for the number of paired categories (three). The binary accuracy averaged across the three pairs was also tested against the chance level (50%) by one-sided one-sample t -tests with Bonferroni correction for the number of tests (higher visual area, early visual area, and all electrodes; Fig. 3b). Differences among the binary accuracies of the higher visual and early visual areas were tested by two-sided Welch's t -test (Fig. 3b).

Three-choice accuracy during the real-time feedback task was tested using a permutation test. Because the accuracy was expected to be higher than the chance level when the feedback image was under control of the subjects, a one-sided

permutation test was performed. The chance-level distribution of the three-choice accuracy was estimated by shuffling target categories of all trials 1 million times.

To find components that were significantly controlled during the real-time feedback task, the Fisher z-transformed and subject-averaged projected correlation coefficients ($\{z(\overline{PrjR^k(V_{online}, V_{target})})\}$) were evaluated using two-sided permutation tests (Fig. 5g).

The permutations were performed 1 million times by shuffling the target categories of all trials. The α -level was adjusted by Bonferroni correction for the number of principal components that could be decoded significantly better than chance in the open-loop condition.

For each semantic vector of word (v_{word}) and landscape ($v_{landscape}$), the distribution of Pearson's correlation coefficients between the inferred vectors ($v_{inferred}$) and the semantic vector was evaluated for its difference between the non-imagery and imagery periods. Because it was hypothesized that these correlation coefficients would increase during imagery, the Fisher z-transformed correlation coefficients for the non-imagery and imagery periods were tested using one-sided Welch's t -test (Fig. 7a and Supplementary Fig. 6b).

Among all nine subjects who participated in both the video-watching task and the imagery task, ΔZ_{word} and $\Delta Z_{landscape}$ using high- γ features was tested against no modulation (0). Because it was hypothesized that these modulations would become positive, one-sided one-sample t -tests were adopted for the test. The α -level was adjusted by Bonferroni correction for the number of tests (six) (Fig. 7c).

References

1. Winlove, C.I.P. et al. The neural correlates of visual imagery: A co-ordinate-based meta-analysis. *Cortex* **105**, 4-25 (2018).
2. Pearson, J. The human imagination: The cognitive neuroscience of visual mental imagery. *Nat Rev Neurosci* **20**, 624-634 (2019).
3. Kastner, S., De Weerd, P., Desimone, R. & Ungerleider, L.G. Mechanisms of directed attention in the human extrastriate cortex as revealed by functional MRI. *Science* **282**, 108-111 (1998).
4. Miyawaki, Y. et al. Visual image reconstruction from human brain activity using a combination of multiscale local image decoders. *Neuron* **60**, 915-929 (2008).
5. Shen, G., Horikawa, T., Majima, K. & Kamitani, Y. Deep image reconstruction from human brain activity. *PLoS Comput Biol* **15**, e1006633 (2019).
6. Naselaris, T., Prenger, R.J., Kay, K.N., Oliver, M. & Gallant, J.L. Bayesian reconstruction of natural images from human brain activity. *Neuron* **63**, 902-915 (2009).
7. Nishida, S. & Nishimoto, S. Decoding naturalistic experiences from human brain activity via distributed representations of words. *NeuroImage* **180**, 232-242 (2018).
8. Nishimoto, S. et al. Reconstructing visual experiences from brain activity evoked by natural movies. *Curr Biol* **21**, 1641-1646 (2011).
9. Naselaris, T., Olman, C.A., Stansbury, D.E., Ugurbil, K. & Gallant, J.L. A voxel-wise encoding model for early visual areas decodes mental images of remembered scenes. *NeuroImage* **105**, 215-228 (2015).
10. Horikawa, T. & Kamitani, Y. Generic decoding of seen and imagined objects using hierarchical visual features. *Nat Commun* **8**, 15037 (2017).
11. Breedlove, J.L., St-Yves, G., Olman, C.A. & Naselaris, T. Generative feedback explains distinct brain activity codes for seen and mental images. *Curr Biol* **30**, 2211-2224 e2216 (2020).
12. Kamitani, Y. & Tong, F. Decoding the visual and subjective contents of the human brain. *Nat Neurosci* **8**, 679-685 (2005).
13. Cukur, T., Nishimoto, S., Huth, A.G. & Gallant, J.L. Attention during natural vision warps semantic representation across the human brain. *Nat Neurosci* **16**, 763-770 (2013).
14. Pearson, J., Clifford, C.W. & Tong, F. The functional impact of mental imagery on conscious perception. *Curr Biol* **18**, 982-986 (2008).
15. Pearson, J., Naselaris, T., Holmes, E.A. & Kosslyn, S.M. Mental imagery: Functional mechanisms and clinical applications. *Trends Cogn Sci* **19**, 590-602 (2015).
16. Yanagisawa, T. et al. Electrographic control of a prosthetic arm in paralyzed patients. *Ann Neurol* **71**, 353-361 (2012).
17. Liu, H., Agam, Y., Madsen, J.R. & Kreiman, G. Timing, timing, timing: Fast decoding of object information from intracranial field potentials in human visual cortex. *Neuron* **62**, 281-290 (2009).
18. Wang, W., Degenhart, A.D., Sudre, G.P., Pomerleau, D.A. & Tyler-Kabara, E.C. Decoding semantic information from human electrocorticographic (ECoG) signals. *Conf Proc IEEE Eng Med Biol Soc* **2011**, 6294-6298 (2011).

19. Rupp, K. et al. Semantic attributes are encoded in human electrocorticographic signals during visual object recognition. *NeuroImage* **148**, 318-329 (2017).
20. Mikolov, T., Sutskever, I., Chen, K., Corrado, G. & Dean, J. Distributed representations of words and phrases and their compositionality. *Proceedings of the 26th International Conference on Neural Information Processing Systems* **2**, 3111-3119 (2013).
21. Koide-Majima, N., Nakai, T. & Nishimoto, S. Distinct dimensions of emotion in the human brain and their representation on the cortical surface. *NeuroImage* **222**, 117258 (2020).
22. Nakai, T., Koide-Majima, N. & Nishimoto, S. Correspondence of categorical and feature-based representations of music in the human brain. *Brain Behav* **11**, e01936 (2021).
23. Cerf, M. et al. On-line, voluntary control of human temporal lobe neurons. *Nature* **467**, 1104-1108 (2010).
24. Watanabe, T., Sasaki, Y., Shibata, K. & Kawato, M. Advances in fMRI real-time neurofeedback. *Trends Cogn Sci* **21**, 997-1010 (2017).
25. Yaffe, R.B., Shaikhouni, A., Arai, J., Inati, S.K. & Zaghoul, K.A. Cued memory retrieval exhibits reinstatement of high gamma power on a faster timescale in the left temporal lobe and prefrontal cortex. *J Neurosci* **37**, 4472-4480 (2017).
26. Berezutskaya, J. et al. Cortical network responses map onto data-driven features that capture visual semantics of movie fragments. *Sci Rep* **10**, 12077 (2020).
27. Fukuma, R. et al. Decoding visual stimulus in semantic space from electrocorticography signals. *IEEE Sys Man Cybern*, 102-104 (2018).
28. Garrard, P., Ralph, M.A., Hodges, J.R. & Patterson, K. Prototypicality, distinctiveness, and intercorrelation: Analyses of the semantic attributes of living and nonliving concepts. *Cogn Neuropsychol* **18**, 125-174 (2001).
29. Ruts, W. et al. Dutch norm data for 13 semantic categories and 338 exemplars. *Behav Res Methods Instrum Comput* **36**, 506-515 (2004).
30. Binder, J.R. et al. Toward a brain-based componential semantic representation. *Cogn Neuropsychol* **33**, 130-174 (2016).
31. Pennington, J., Socher, R. & Manning, C.D. Glove: Global vectors for word representation. *Proceedings of the 2014 conference on empirical methods in natural language processing (EMNLP)*, 1532-1543 (2014).
32. Pereira, F., Gershman, S., Ritter, S. & Botvinick, M. A comparative evaluation of off-the-shelf distributed semantic representations for modelling behavioural data. *Cogn Neuropsychol* **33**, 175-190 (2016).
33. Reddy, L., Tsuchiya, N. & Serre, T. Reading the mind's eye: Decoding category information during mental imagery. *NeuroImage* **50**, 818-825 (2010).
34. Johnson, M.R. & Johnson, M.K. Decoding individual natural scene representations during perception and imagery. *Front Hum Neurosci* **8**, 59 (2014).
35. Murguialday, A.R. et al. Transition from the locked in to the completely locked-in state: A physiological analysis. *Clinical Neurophysiology* **122**, 925-933 (2011).
36. Wolpaw, J.R., Birbaumer, N., McFarland, D.J., Pfurtscheller, G. & Vaughan, T.M. Brain-computer interfaces for communication and control. *Clin Neurophysiol* **113**, 767-791 (2002).

37. Kageyama, Y. et al. Severely affected ALS patients have broad and high expectations for brain-machine interfaces. *Amyotroph Lat Scl Fr* **15**, 513-519 (2014).
38. Pandarinath, C. et al. High performance communication by people with paralysis using an intracortical brain-computer interface. *eLife* **6** (2017).
39. Vansteensel, M.J. et al. Fully implanted brain-computer interface in a locked-in patient with ALS. *N Engl J Med* **375**, 2060-2066 (2016).
40. Morris, S. et al. Patient-specific cortical electrodes for sulcal and gyral implantation. *IEEE Trans Biomed Eng* **62**, 1034-1041 (2015).
41. Geser, F. et al. Evidence of multisystem disorder in whole-brain map of pathological TDP-43 in amyotrophic lateral sclerosis. *Arch Neurol* **65**, 636-641 (2008).
42. deBettencourt, M.T., Cohen, J.D., Lee, R.F., Norman, K.A. & Turk-Browne, N.B. Closed-loop training of attention with real-time brain imaging. *Nat Neurosci* **18**, 470-475 (2015).
43. Deng, J. et al. ImageNet: A large-scale hierarchical image database. *Proc CVPR IEEE*, 248-255 (2009).
44. Kudo, T., Yamamoto, K. & Matsumoto, Y. Applying conditional random fields to Japanese morphological analysis. *Proceedings of the 2004 Conference on Empirical Methods in Natural Language Processing*, 230-237 (2004).
45. Mikolov, T., Chen, K., Corrado, G. & Dean, J. Efficient estimation of word representations in vector space. *Preprint at arXiv:1301.3781* (2013).
46. Mikolov, T., Yih, W.-t. & Zweig, G. Linguistic regularities in continuous space word representations. *Proceedings of the 2013 conference of the north american chapter of the association for computational linguistics: Human language technologies*, 746-751 (2013).
47. Chi, T., Ru, P. & Shamma, S.A. Multiresolution spectrotemporal analysis of complex sounds. *J Acoust Soc Am* **118**, 887-906 (2005).
48. Thomas, E., Dyson, M. & Clerc, M. An analysis of performance evaluation for motor-imagery based BCI. *J Neural Eng* **10**, 031001 (2013).
49. Kriegeskorte, N., Simmons, W.K., Bellgowan, P.S. & Baker, C.I. Circular analysis in systems neuroscience: The dangers of double dipping. *Nat Neurosci* **12**, 535-540 (2009).
50. Delorme, A. & Makeig, S. EEGLAB: An open source toolbox for analysis of single-trial EEG dynamics including independent component analysis. *J Neurosci Methods* **134**, 9-21 (2004).
51. Dale, A.M., Fischl, B. & Sereno, M.I. Cortical surface-based analysis. I. Segmentation and surface reconstruction. *NeuroImage* **9**, 179-194 (1999).
52. Papademetris, X. et al. BioImage Suite: An integrated medical image analysis suite: An update. *Insight J* **2006**, 209 (2006).
53. Groppe, D.M. et al. iELVis: An open source MATLAB toolbox for localizing and visualizing human intracranial electrode data. *J Neurosci Methods* **281**, 40-48 (2017).
54. Glasser, M.F. et al. A multi-modal parcellation of human cerebral cortex. *Nature* **536**, 171-178 (2016).

Acknowledgments: We thank all subjects for their participation. **Funding:** This research was conducted under the Japan Science and Technology Agency (JST) Core Research for Evolutional Science and Technology (JPMJCR18A5). This research was also supported in part by the JST Precursory Research for Embryonic Science and Technology (JPMJPR1506), Exploratory Research for Advanced Technology (JPMJER1801), Moonshot R&D (JPMJMS2012), Grants-in-Aid for Scientific Research from KAKENHI (JP26560467, JP17H06032, JP20K16466, JP15H05710, JP18H04085, 20H05705 and JP18H05522), Grants from the Japan Agency for Medical Research and Development (AMED) (19dm0207070h0001, 19dm0307103, 19de0107001 and 19dm0307008), and the Canon Foundation. **Author contributions:** Conceptualization: T.Y.; Methodology: R.F. and T.Y.; Investigation: R.F., T.Y., H.S., K.T., S.Y., Y.I., Y.F., S.O., N.T., and N.K.–M.; Data curation, formal analysis, and software: R.F.; Funding acquisition: R.F., T.Y., and H.K.; Writing—original draft: R.F. and T.Y.; Writing—review and editing: R.F., T.Y., S.N., Y.K., and H.K.; Supervision: T.Y. **Competing interests:** The authors declare no competing interests. **Data and materials availability:** All data are available in the main text, or the supplementary materials.

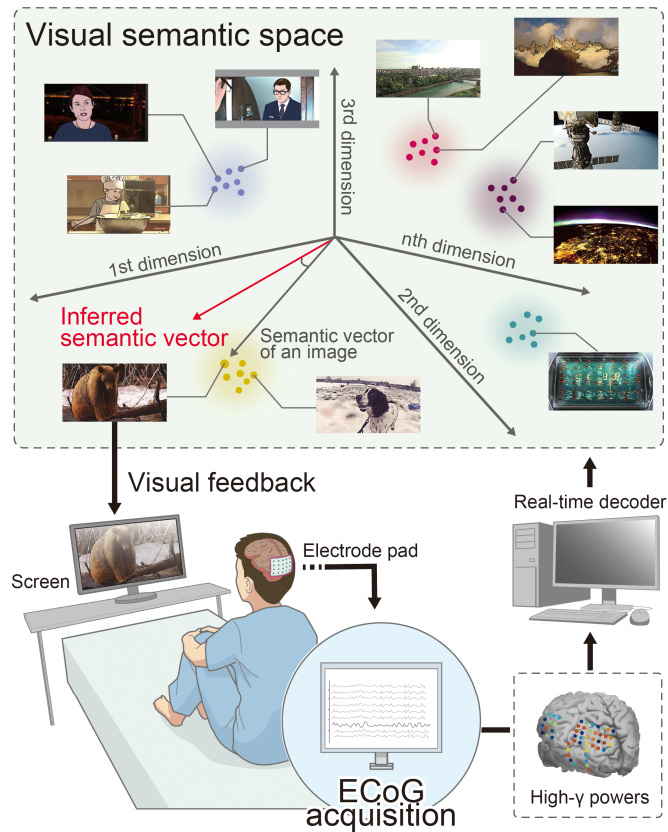


Fig. 1. Schematic of a closed-loop system. ECoGs were acquired in real time to infer a semantic vector of 1,000 dimensions in the visual semantic space from power in the high- γ band. An image that had the nearest semantic vector to the inferred semantic vector was presented to the subject as a feedback image.

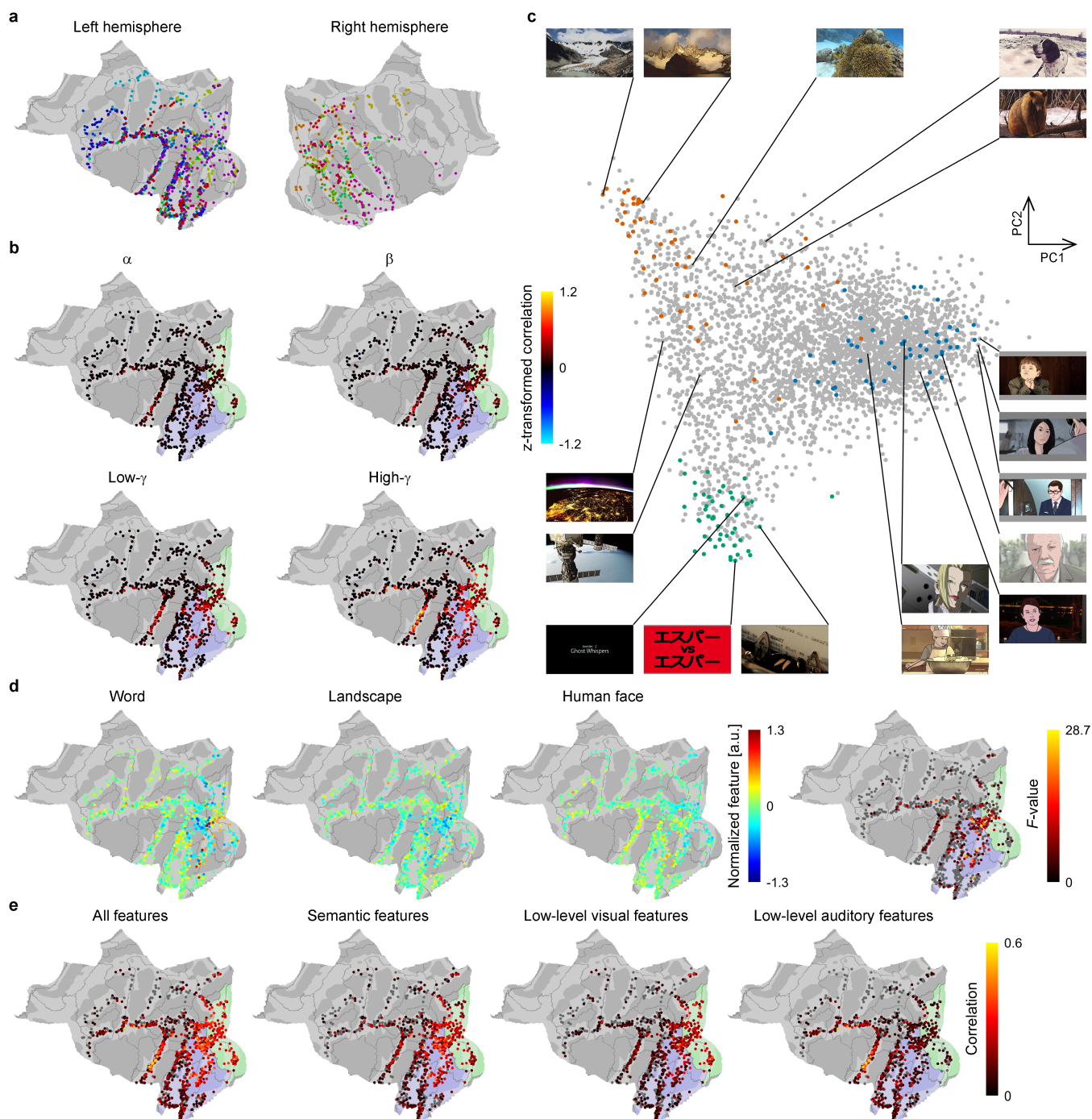


Fig. 2. Visual semantic space and high- γ powers/features in the open-loop

condition. (a) Locations of subdural electrodes are color-coded for each subject who participated in this study ($n = 21$). (b) The Fisher z-transformed Pearson's correlation coefficients between the 150 powers corresponding to repeated 2.5-min movies in the validation video were averaged across all possible combinations of the repetitions to be color-coded on each electrode. Areas shaded with blue and green denote the higher

and early visual areas, respectively. (c) Each scene is shown at a position based on the first and second principal components (PCs) of the semantic vectors. Green, red, and blue points represent the positions of 50 scenes selected as representative of the categories of “word”, “landscape”, and “human face”, respectively. Illustrations are shown instead of the actual images used in the task. (d) The high- γ features corresponding to the 50 selected scenes from the three categories were averaged within each category and color-coded at the location of the electrodes. For visibility, features of each electrode were z-scored within 3,600 scenes. The F -values of ANOVA for the high- γ features were similarly color-coded at each electrode ($P < 0.05$, $n = 50$ for each group, uncorrected one-way ANOVA). (e) Pearson’s correlation coefficients between the high- γ features during watching the training videos and those inferred from the semantic vectors (semantic features), and the low-level visual and auditory features of the videos were color-coded and shown at the location of the electrode. In the analysis, decoders were first trained to infer high- γ features using all features from the videos; to create a correlation map of each feature set, the weights corresponding to the other two feature sets were set to zero before regression. Only electrodes that showed significant positive correlations are shown ($P < 0.05$, $n = 3,600$ for each electrode, uncorrected one-sided Pearson’s correlation test).

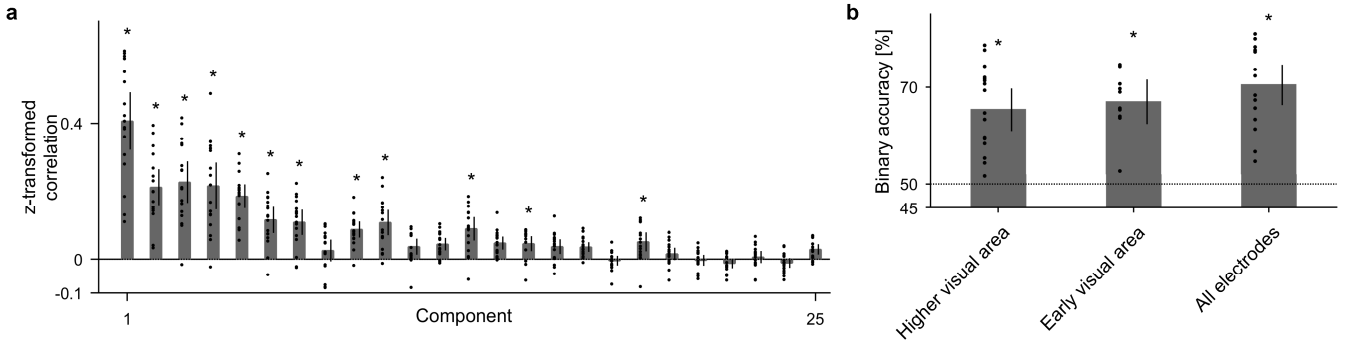


Fig. 3. Decoding accuracy in the open-loop condition.

(a) $PrjR^k(V_{inferred}, V_{true})$ was Fisher z-transformed and averaged across the 17 subjects ($\overline{z(PrjR^k(V_{inferred}, V_{true}))}$), which is shown in the order of principal components. For visibility, the first 25 components are shown (for all components, see Supplementary Fig. 3b). Individual values are shown with dots. Error bars denote 95% CIs among the subjects. $*P < 0.5 \times 10^{-4}$ (Bonferroni-adjusted α -level; 0.05/1,000), two-sided permutation test. (b) Binary classification accuracies for all three pairs from the three categories (word, landscape, and human face) were averaged to show the subject-averaged binary classification accuracy with the bars. Individual values are shown with dots. Error bars denote 95% CIs among subjects. The accuracy was calculated based on the semantic vectors inferred from high- γ features from higher visual area ($n = 17$), early visual area ($n = 10$), and all implanted electrodes ($n = 17$). There was no significant difference between the accuracies based on the higher and early visual areas ($P = 0.5767$, $t(23.3) = -0.57$, uncorrected two-sided Welch's t -test). $*P < 1.7 \times 10^{-2}$ (Bonferroni-adjusted α -level; 0.05/3), one-sided one-sample t -test against chance level (50%).

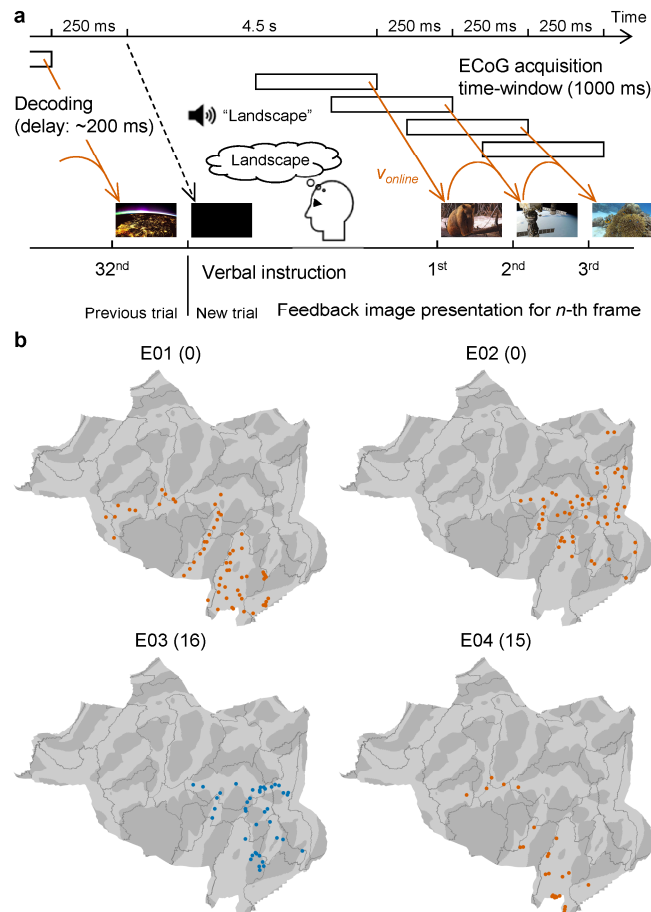


Fig. 4. Real-time feedback task. (a) Timing of ECoG acquisition and feedback image presentation during the real-time feedback task is shown with a schematic. Immediately after delivery of the instruction, 1,000-ms ECoGs were acquired while the subject was watching the black screen to infer the semantic vector in real-time (online vector: v_{online}) with the online decoder. Next, the first feedback image was selected from among the images in the training videos based on the highest $R(v_{online}, v_{true}^i)$ and presented to the subject. Then, successive 1,000-ms ECoGs were acquired every 250 ms to calculate the next online vector (v_{online}), which was the linear interpolation between the inferred vector from the ECoGs and the previous online vector. A total of 32 feedback images were presented for each instruction. The order of instructions was randomized. The system delay from the end of the acquisition to the image presentation was approximately 200 ms. All four subjects participated in

four sessions of 30 trials each, with breaks between sessions to minimize their fatigue.

(b) Locations of subdural electrodes used for decoding in the real-time feedback task are mapped on a normalized brain surface. Red and blue markers denote electrodes in the left and right hemispheres, respectively. The number of depth electrodes used in the real-time decoding is shown in parentheses.

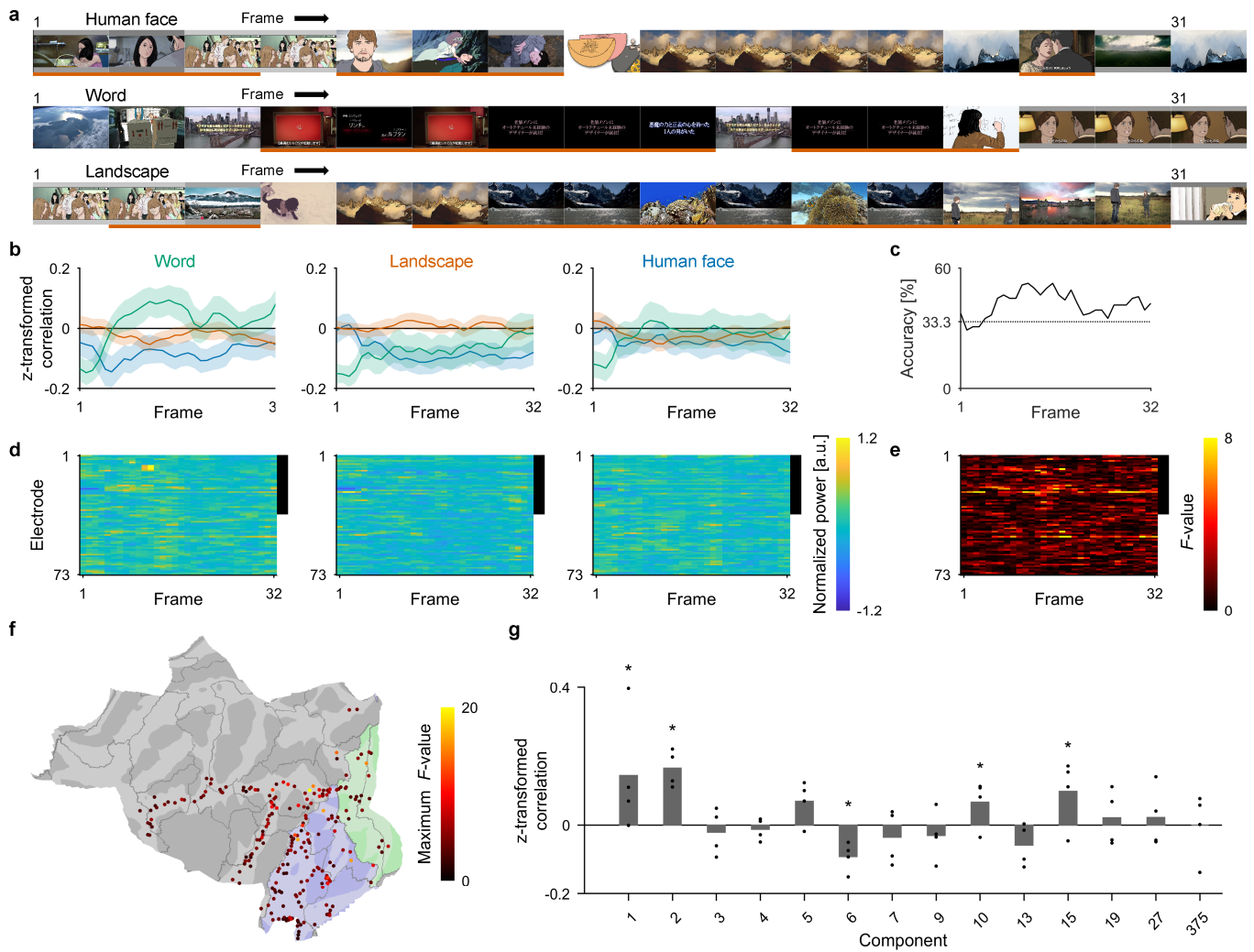


Fig. 5. Closed-loop performance in controlling the inferred images. (a)

Representative feedback images are shown for E01 during trials 28 to 30 of the first session with the corresponding target categories shown on the top. Due to the figure size, one of every two images is shown. The images underlined in red are the correct decoding in the context of a three-choice task in each frame. (b) For E01, the trial-averaged $z(R(v_{online}, v_{category}))$, where ($v_{category} : v_{word}, v_{landscape}, \text{ or } v_{face}$), are shown as green, red and blue lines, respectively, with 95% CIs by shaded area. The title of each panel indicates the target categories for the averaged trials. (c) The three-choice accuracy at each frame is shown. Dotted line denotes chance level (33.3%). (d) Power in the high- γ band during the feedback trials for each target category were averaged to be color-coded for each electrode and frame. The black line on the right side of the

plot indicates the electrodes in the higher visual area. For visualization, the powers were z-scored across all trials and frames for each electrode. (e) For each electrode and frame, F -values of one-way ANOVA across the high- γ powers during the three target categories in (d) were color-coded. The black line on the right side of the plot indicates the electrodes in the higher visual area. (f) For four subjects (E01–E04), the maximum F -values of the high- γ powers in (e) were color-coded at the location of each electrode. (g) $PrjR^k(V_{online}, V_{target})$

($V_{online} := \{v_{online}^{i,j}\}$ and $V_{target} := \{v_{target}^{i,j}\}$ where $i = 1, \dots, 120$ (trial); $j = 1, \dots, 32$ (frame)) were

Fisher z-transformed and averaged across all four subjects to be shown in order of the principal components. Here, $PrjR^k(V_{online}, V_{target})$ was evaluated only for the 14

principal components whose $\overline{z(PrjR^k(V_{inferred}, V_{true}))}$ was positively significant in the

open-loop condition. The $\overline{z(PrjR^k(V_{online}, V_{target}))}$ was compared with the

corresponding chance distribution for each component (k)

($\overline{z(PrjR^k(V_{online}, \{v_{target}^{i,j}\}))}$ where i is shuffled (1, ..., 120); $j = 1, \dots, 32$). Individual values

are shown with dots. $*P < 3.6 \times 10^{-3}$ (Bonferroni-adjusted α -level; 0.05/14), two-sided permutation test.

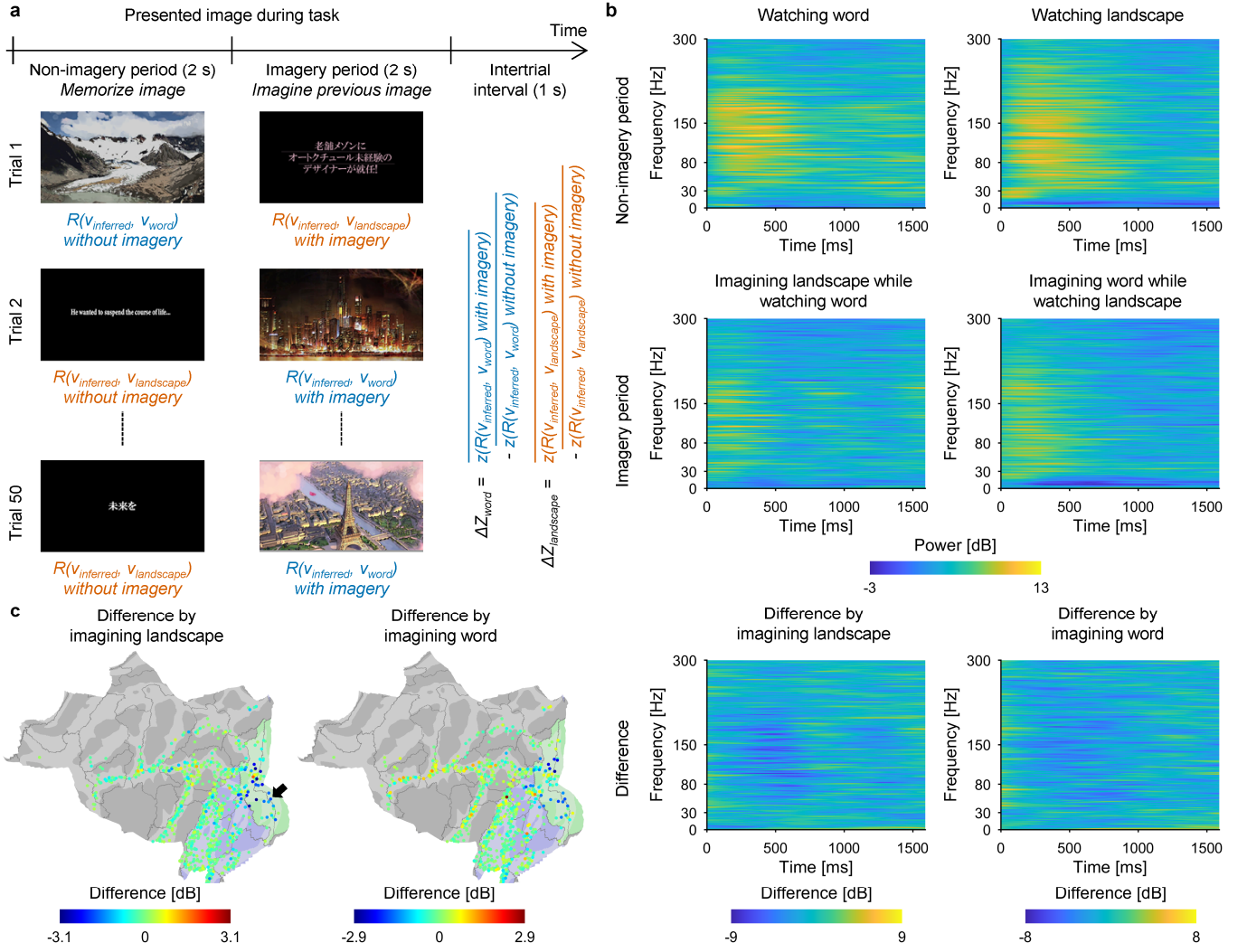


Fig. 6. ECoGs during the imagery task. (a) Schematic of the imagery task. After presentation of the word or landscape image (non-imagery period), the subjects imagined the word image during presentation of the landscape image, or imagined the landscape image during presentation of the word image (imagery period). For all combinations of images, the trials were repeated in randomized order, resulting in 50 trials. To obtain modulation of $R(v_{inferred}, v_{word})$ due to imagining the word image (ΔZ_{word}), the $R(v_{inferred}, v_{word})$ during the presentations of landscape images were Fisher z-transformed and averaged within the non-imagery period and the imagery period to calculate the difference between them ($\overline{z(R(v_{inferred}, v_{word}))}$ during imagery period $- \overline{z(R(v_{inferred}, v_{word}))}$ during non-imagery period). Similarly, $\Delta Z_{landscape}$ was

evaluated from the $R(v_{inferred}, v_{landscape})$ during the presentation of word images. (b) Results of time-frequency decomposition for the ECoGs of the electrode indicated by the black arrow in (c). The upper and middle panels represent the time-frequency maps of ECoGs while watching the image of words (left) and landscapes (right) during the non-imagery period and imagery period, respectively. The difference between these two maps of each column is shown in the bottom panel. (c) Powers in the high- γ band from 0 to 1 s after the presentation of word images (left) and landscape images (right) were subtracted between the two periods (imagery period – non-imagery period) to be shown on the cortical surface at the location of each subdural electrode with color coding.

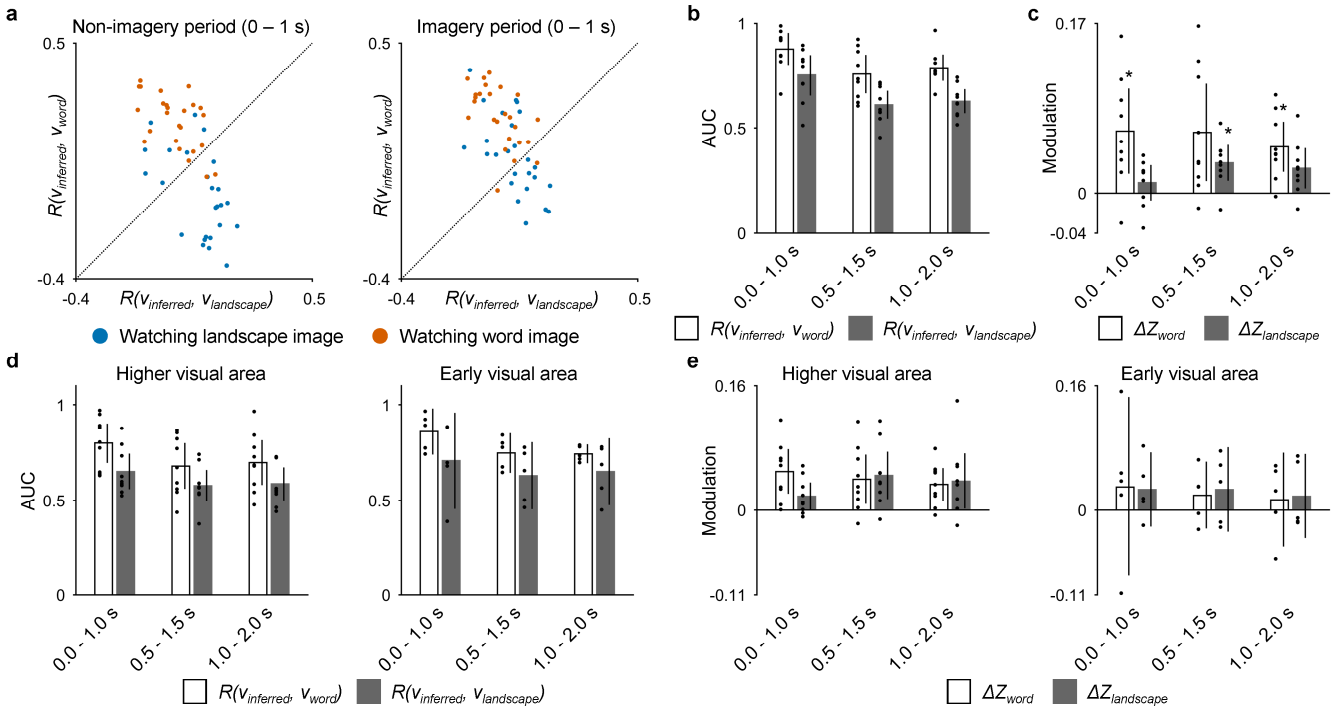


Fig. 7. Modulation of the inferred semantic vectors by mental imagery. (a) The $R(v_{inferred}, v_{word})$ (vertical axis) and the $R(v_{inferred}, v_{landscape})$ (horizontal axis) for each image were plotted with color-coded (blue, presentation of landscape image; red, presentation of word image) points for E01. (b) For each 1-s time window, the AUC to identify the category of the presented image (word or landscape) in the non-imagery period solely using $R(v_{inferred}, v_{word})$ or $R(v_{inferred}, v_{landscape})$ is shown with white and black bars, respectively. Individual values are shown with dots. Error bars denote the 95% CIs among subjects ($n = 9$). (c) ΔZ_{word} and $\Delta Z_{landscape}$ averaged across the subjects ($n = 9$) are shown with white and black bars, respectively, for each 1-s time window. Individual values are shown with dots. Error bars denote 95% CIs among subjects. $*P < 0.0083$ (Bonferroni-adjusted α -level; $0.05/6$), one-sided one-sample t -test. (d) For each of three 1-s time windows in the non-imagery period, the AUC to identify the category of the presented image based on $R(v_{inferred}, v_{word})$ or $R(v_{inferred}, v_{landscape})$ is shown from using the high- γ features from the higher visual area (left; $n = 9$) and early visual area (right; $n = 5$). Individual values are shown with dots.

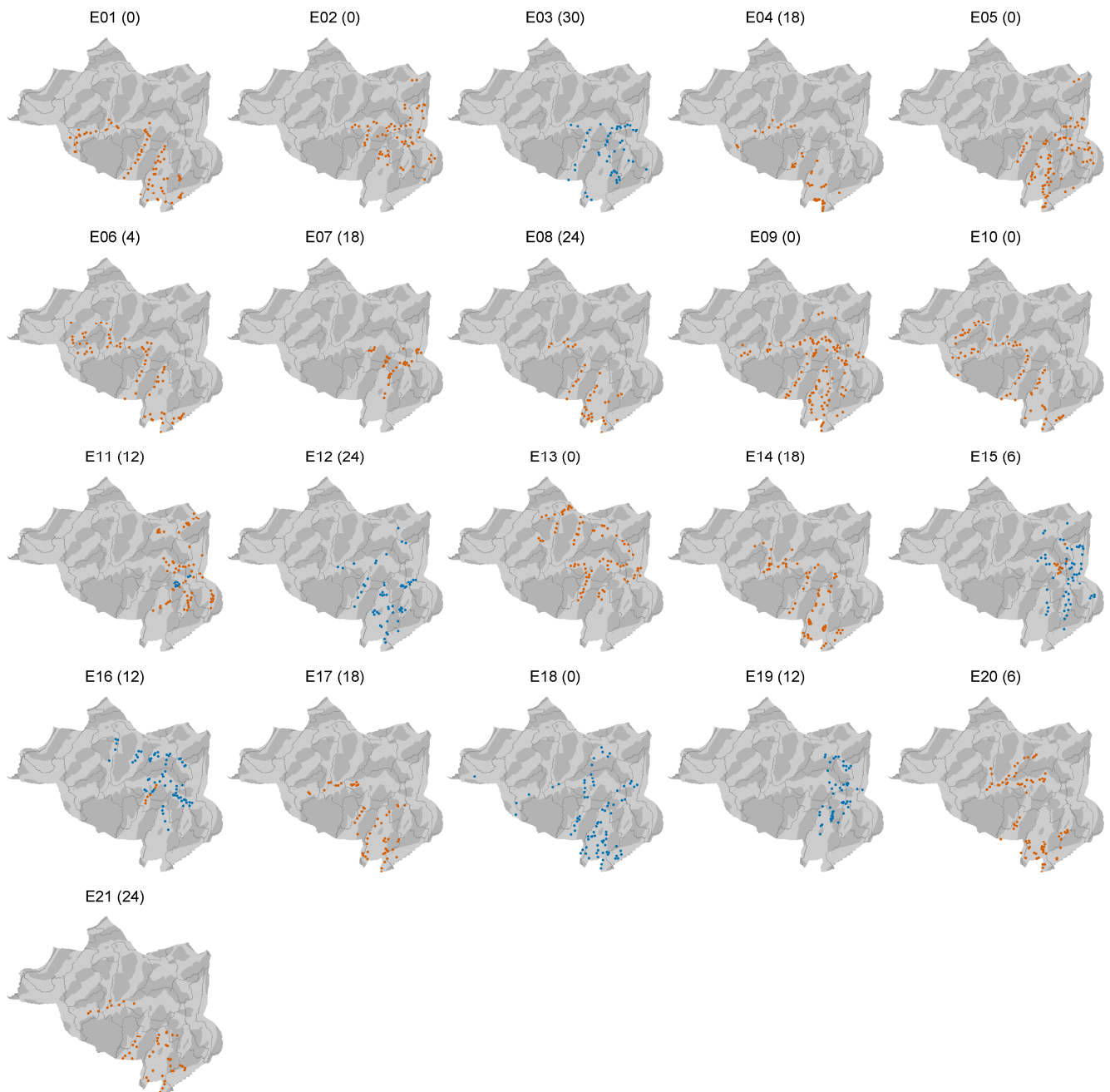
Error bars denote 95% CIs among subjects. (e) For each 1-s time window and for the high- γ features from higher visual area (left; $n = 9$) and early visual area (right; $n = 5$), ΔZ_{word} and $\Delta Z_{landscape}$ averaged across the subjects are shown with white and black bars, respectively. Individual values are shown with dots. Error bars denote 95% CIs among subjects.

Supplementary Materials for

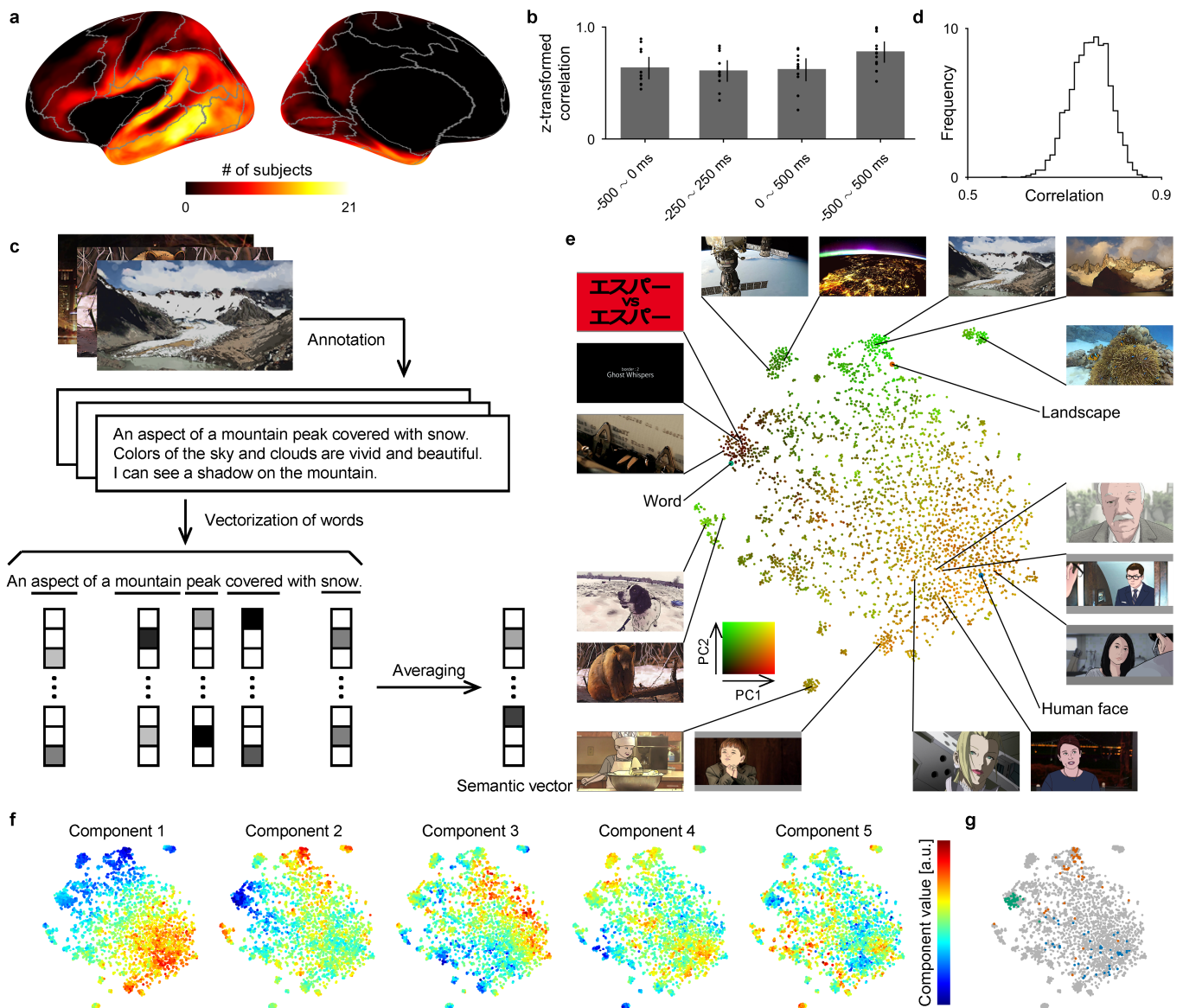
Voluntary control of semantic neural representations by imagery
with conflicting visual stimulation

This PDF file includes the following:

Supplementary Figs. 1 to 6
Supplementary Tables 1 to 3



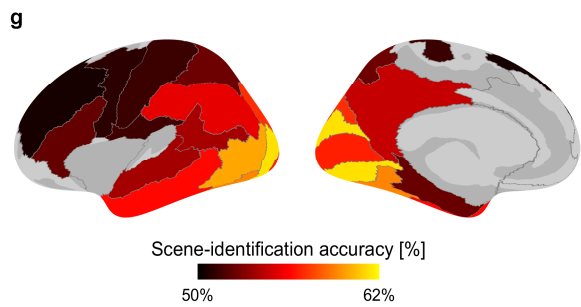
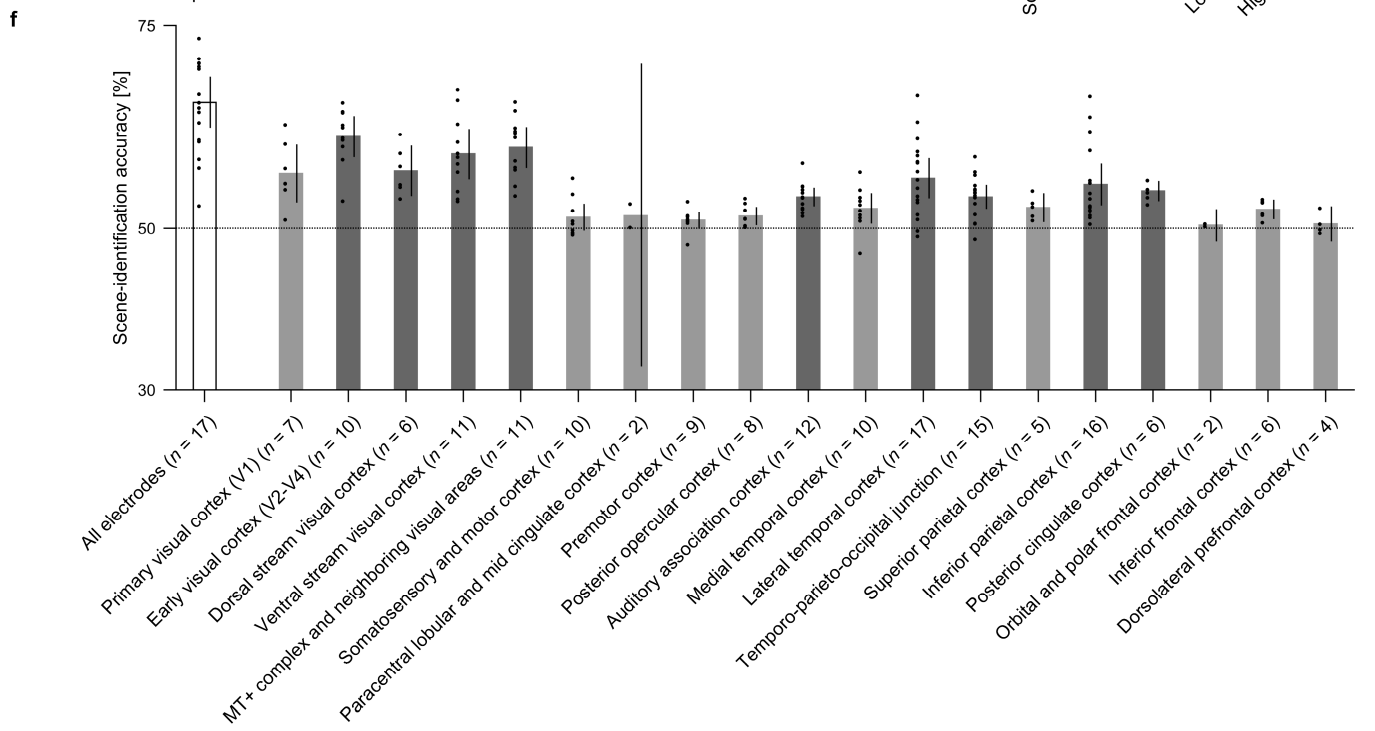
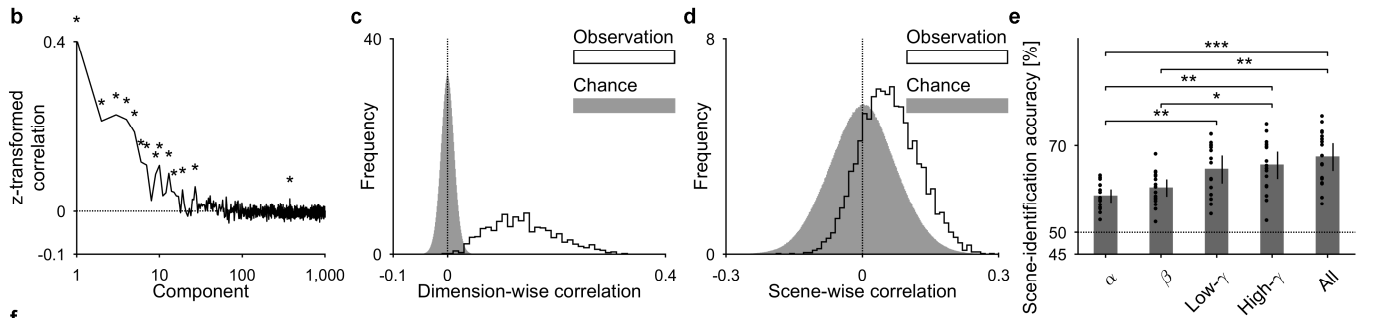
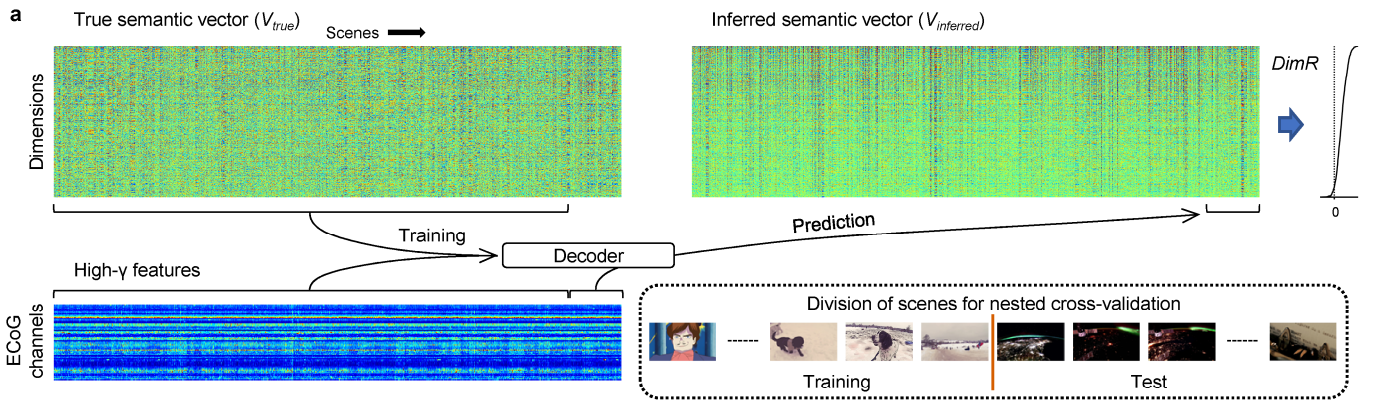
Supplementary Fig. 1. Individual locations of the electrodes. Locations of subdural electrodes for each subject are mapped on a normalized brain surface with red and blue color coding that denote electrodes in the left and right hemispheres, respectively. The number of depth electrodes is shown in parentheses.



Supplementary Fig. 2. Location of electrodes, consistency of power in the high- γ band, and construction of semantic vectors. (a) Electrode coverage across subjects shown in Fig. 2a is color-coded on an inflated normalized brain to show the number of subjects with electrodes at each point. The electrode coverage map was created by averaging the maps of each subject. The locations of all electrodes in a subject were mapped to the left hemisphere of the normalized brain. By using the creepage distance on the pial surface of the template brain, an individual electrode coverage map was created. When a point on the surface of the left hemisphere was located within a distance of 10 mm from any subdural electrode, the coverage value of the point was set to 1; the coverage value of a point located further than 20 mm from all subdural electrodes was set to 0. For a point between these distances, a linearly interpolated value was used according to the minimum distance to any of the subdural electrodes. (b) Subject-averaged consistency of powers in the high- γ band are shown as bars. To calculate the consistency, power in the high- γ band was calculated for all implanted electrodes using each of the time windows. The powers from all electrodes were then concatenated to calculate Pearson's correlation coefficients for all possible pairs across the four repetitions in the validation video; the correlation coefficients were Fisher z-transformed and averaged to acquire one value for a subject (shown as a black dot). Time 0 denotes the

time when images from the validation video were annotated. Error bars denote 95% confidence intervals (CIs) among the subjects. (c) Each still image extracted from the videos was manually annotated and vectorized into semantic vectors using vector representations learned by the skip-gram model. (d) Consistency of semantic vectors across annotators is shown with a histogram. For each scene of the training videos, Pearson’s correlation coefficients were calculated between all pairs of semantic vectors across five annotators (10 pairs) and were averaged within the scene to create the histogram. The mean of the distribution was 0.7523. (e) The dimensionality of the visual semantic space (1,000) was reduced to two dimensions for visualization using t-distributed stochastic neighbor embedding (t-SNE)[†] with the following parameters: number of initial dimensions by principal component analysis (PCA) pre-processing, 30; perplexity of the Gaussian kernel, 30. In addition to the 3,600 semantic vectors of the training videos, vector representations corresponding to “word”, “landscape”, and “human face” were included in the training dataset of the t-SNE. Each scene is shown as a point in the embedded space, with a color corresponding to its first and second principal components (PCs) of the semantic vectors of the training video. Illustrations are presented instead of the actual images used in the task. The green, red, and blue points denote points for vector representations of word, landscape, and human face, respectively. (f) The value of the first five PCs for each scene of the training videos is shown at the point of the embedding space in (e). (g) For the word, landscape, and human face categories, the 50 scenes that had the highest Pearson’s correlation coefficient with their corresponding semantic vector (v_{word} , $v_{landscape}$, or v_{face}) are shown with green, red, and blue markers, respectively, in the embedding space (e).

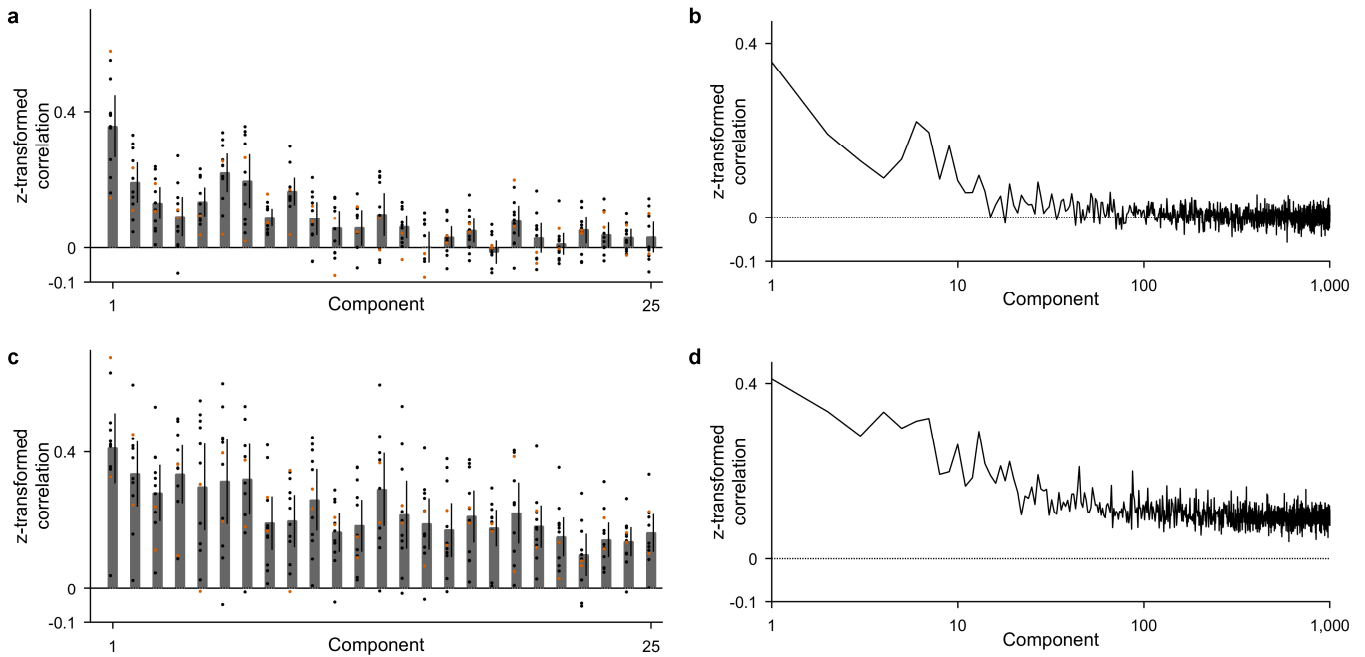
[†] Maaten, L. v. d. & Hinton, G. Visualizing data using t-SNE. *Journal of machine learning research* **9**, 2579-2605 (2008).



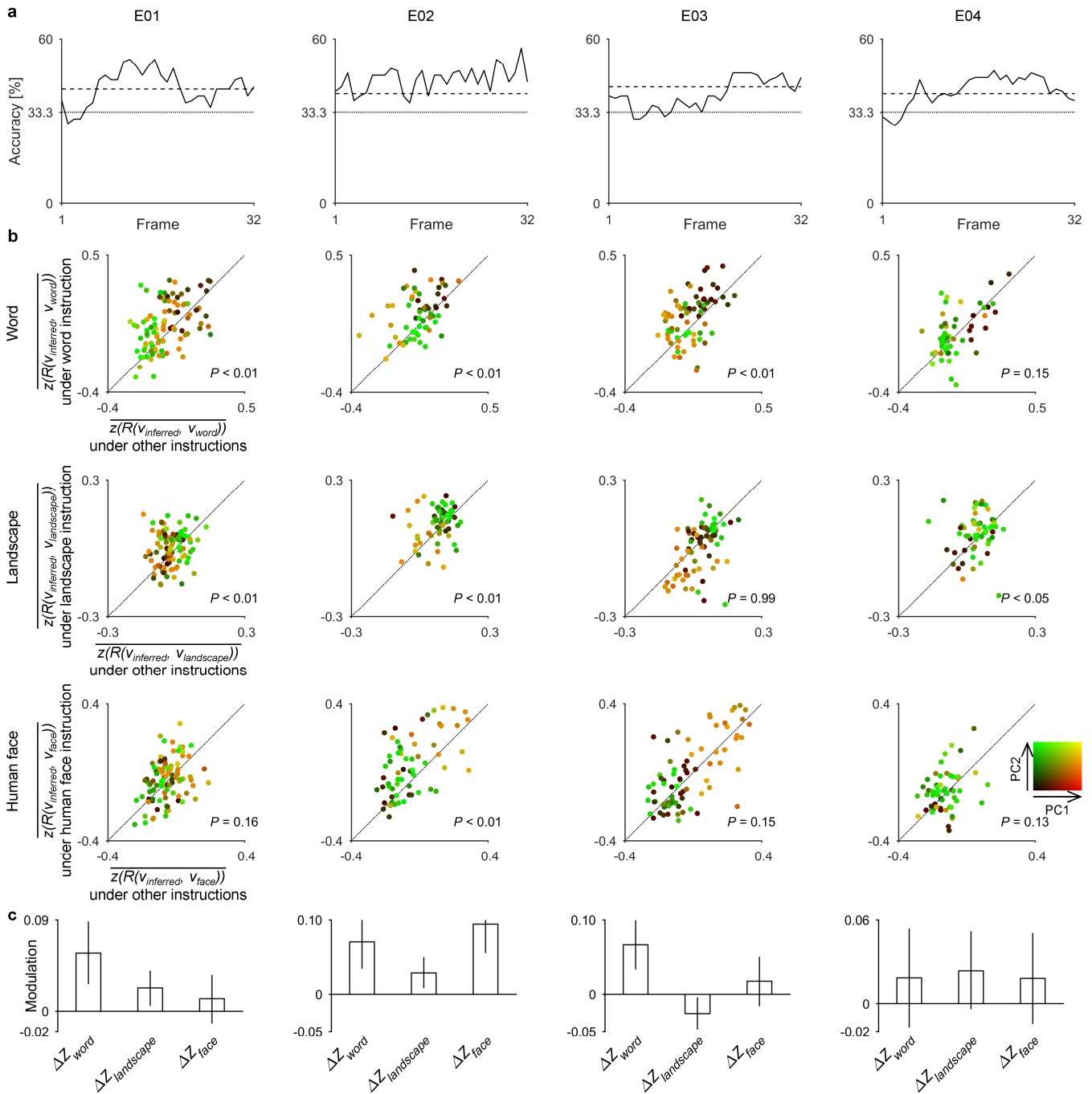
Supplementary Fig. 3. Overview of decoding and decoding accuracy in the open-loop condition.

(a) An overview of the decoding of the semantic vectors using nested cross-validation is illustrated in the schematic. Entire scenes were first divided into 10 groups without overlapping of the scenes between them; during the division, scenes from the same video source were kept in the same dataset so that there were no scenes from the same video source that belonged to multiple groups. Each of these 10 groups was used as a test dataset for decoding, and the other nine groups were used as a training dataset. For each test dataset, a decoder was trained with the high- γ features (left bottom column; representative example of E01) and the true semantic vectors of the training dataset (left upper column) to decode the high- γ features of the test dataset. (b) For each principal component of the true semantic vectors of the training videos, the projected correlation coefficient ($\overline{z(\text{Prj}R^k(V_{\text{inferred}}, V_{\text{true}}))}$) is shown in order of the components. For visibility, the horizontal axis is shown in log space. Asterisks denote principal components that correlated significantly better than chance ($P < 0.5 \times 10^{-4}$ [Bonferroni-adjusted α -level; 0.05/1,000], $n = 17$, two-sided permutation test). (c) For each dimension of the visual semantic space (1,000), Pearson's correlation coefficients were calculated between the true semantic vectors and the inferred semantic vectors using high- γ features to be Fisher z-transformed and averaged across all subjects ($n = 17$) (white). Chance distribution was estimated by shuffling scenes among the true semantic vectors in the same way that the projected correlation coefficients were tested (gray). (d) For each scene, the scene-wise correlation coefficient of each subject was Fisher z-transformed and averaged ($n = 17$) (white). Chance distribution was estimated by shuffling scenes among the true semantic vectors in the same way that the projected correlation coefficients were tested (gray). (e) The subject-averaged scene-identification accuracies for all 3,600 scenes are shown with a bar graph for four frequency bands (α : 8–13 Hz; β : 13–30 Hz; low γ : 30–80 Hz; high γ : 80–150 Hz) and their combinations. For decoding, features from all implanted electrodes were used. The scene-identification accuracy was calculated by comparing the inferred vector of each scene against the true semantic vectors of other scenes in the same test dataset in the nested cross-validation, but scenes originating from the same video source were removed; the scene-identification accuracies for all scenes were then averaged for each subject. Individual values are shown with dots. Error bars denote 95% CIs across subjects. * $P < 0.05$, ** $P < 0.01$, and *** $P < 0.001$ ($P < 0.001$, $n = 17$ for each group, $F(4,80) = 8.55$, one-way analysis of variance [ANOVA] with the post hoc Tukey–Kramer test). (f) Subject-averaged scene-identification accuracies for all 3,600 scenes using high- γ features are shown with a bar graph for each cortical region. Individual values are shown with dots. Error bars denote 95% CIs across subjects. Dark and light bars denote significant and non-significant, respectively, accuracies of the corresponding regions compared to chance (50%) ($P < 2.6 \times 10^{-3}$ [Bonferroni-adjusted α -level; 0.05/19], two-sided one-sample t -test). Scene-identification accuracies using high- γ features significantly differed depending on the cortical region ($P < 0.001$, $F(18,148) = 8.21$, one-way ANOVA with post hoc Tukey–Kramer tests). The scene-identification accuracies were significantly higher for the extrastriate early visual cortex (V2–V4), ventral stream visual cortex, and middle temporal complex and neighboring visual area than for the auditory association cortex ($P < 0.05$) and temporo-parieto-occipital junction ($P < 0.01$). Moreover, the accuracy with the V2–V4 was significantly higher than those with the lateral temporal, inferior parietal, and posterior cingulate cortices ($P < 0.05$). All of the aforementioned regions and the dorsal stream visual cortex showed significant scene-identification accuracies. MT+ complex: middle temporal complex. (g) The scene-identification accuracies averaged across subjects for each region (shown in (f)) were color-

coded and plotted on the surface of the inflated normalized brain, except the regions on which the electrodes were placed in fewer than three subjects.

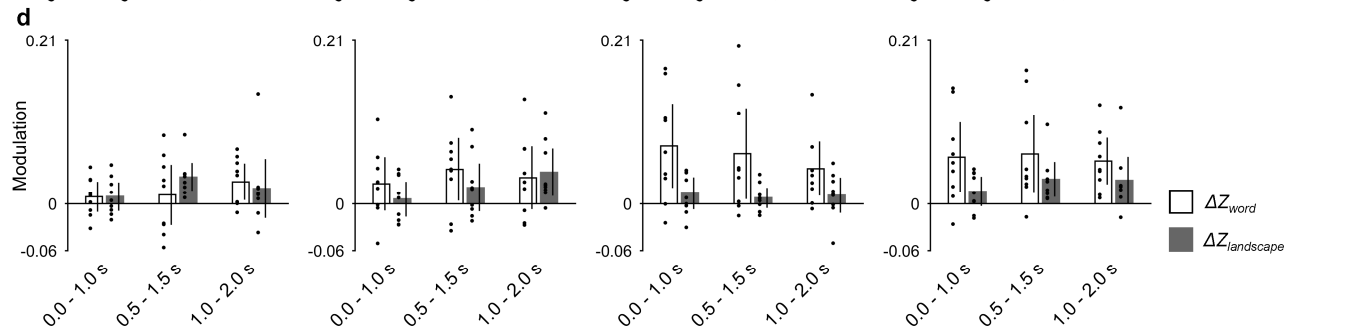
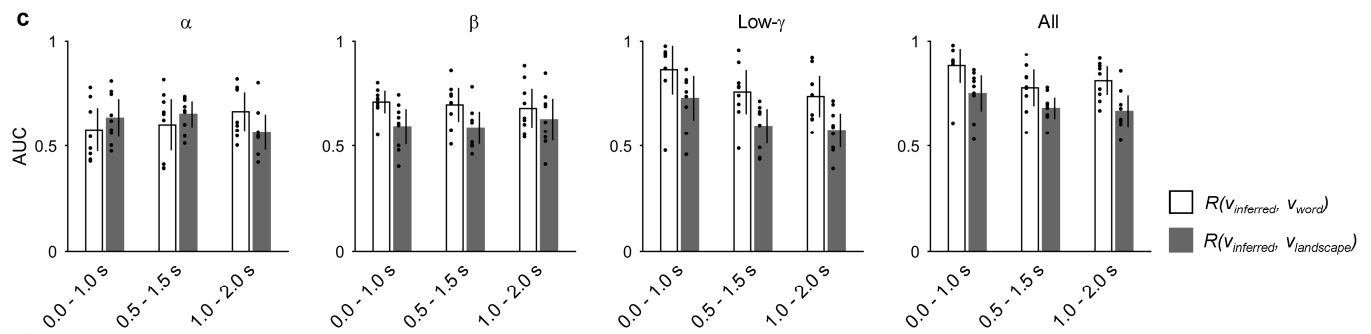
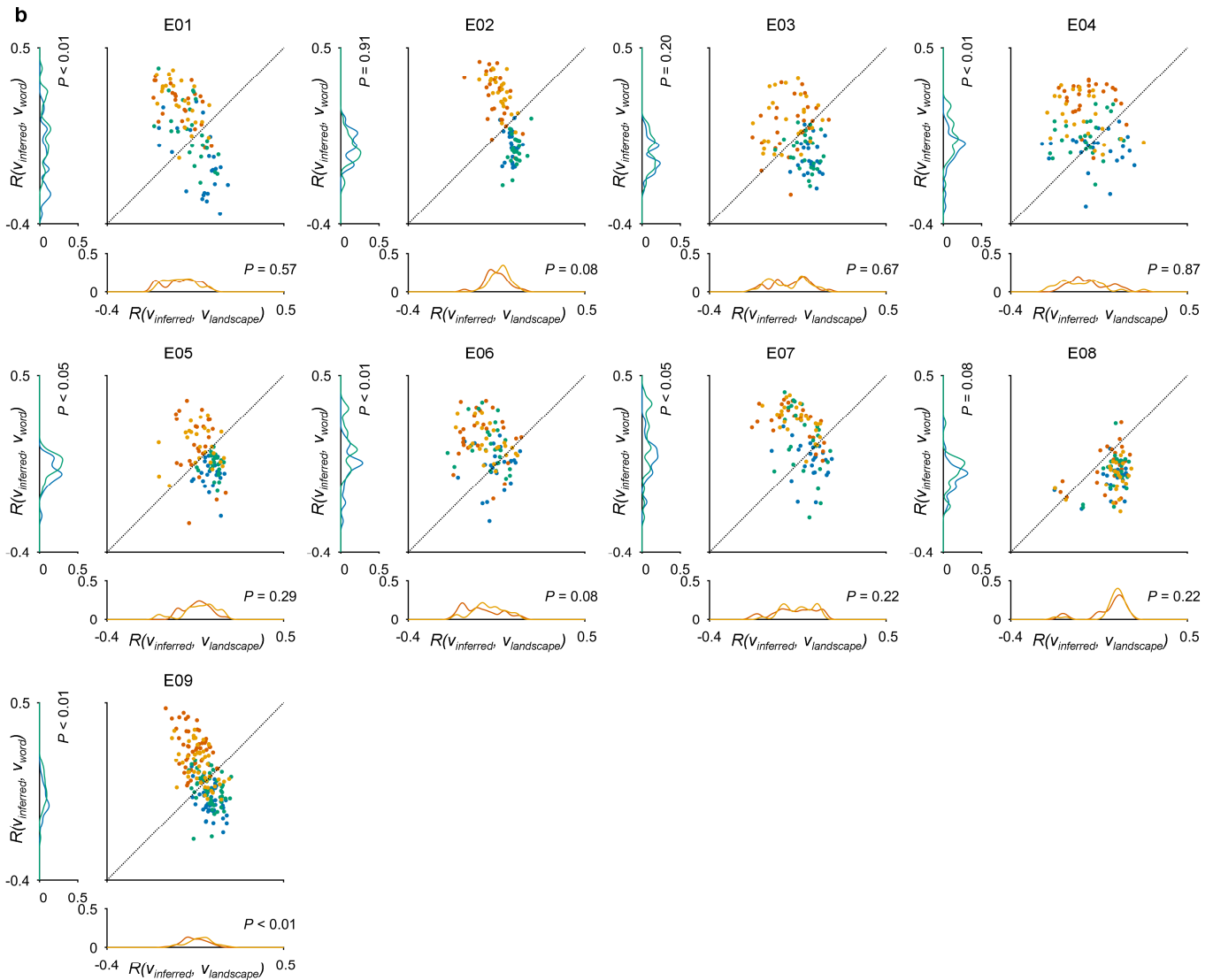
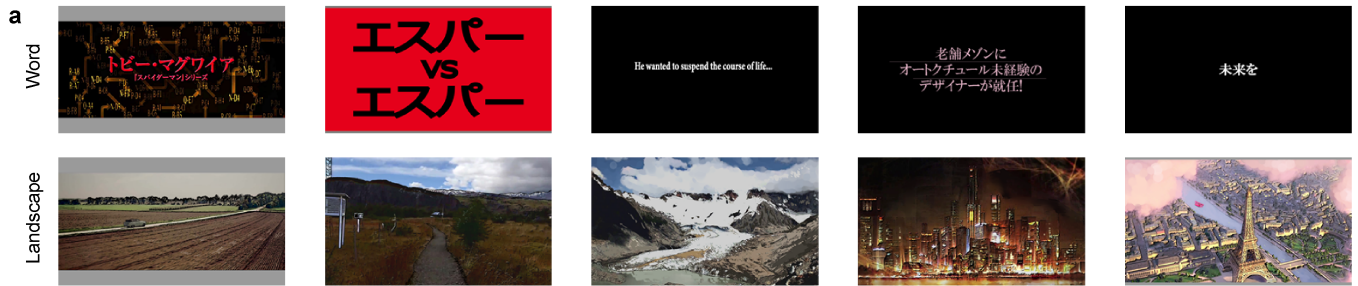


Supplementary Fig. 4. Decoding accuracy and consistency for the validation video. (a, b) From ECoGs obtained while watching the validation video, the high- γ features of each scene were acquired to infer the semantic vectors; then the inferred semantic vectors were evaluated for accuracy and consistency. For E01, the online decoder in the real-time feedback task was used to decode the high- γ features. The online decoder of E03 was re-trained excluding four electrodes that became noisy at the time of validation video presentation. For other subjects, decoders were trained using the high- γ features of all implanted electrodes for all 3,600 scenes of training videos by following the same procedures as the online decoders of E01 and E03. The projected correlation coefficients were evaluated by comparing the inferred vectors against the true semantic vectors of each scene created in exactly the same way as those for the training videos. For the projection, the direction vector of the PCA of the true semantic vectors of the training videos was used. The projected correlation coefficients were Fisher z-transformed and averaged across the subjects to be shown in (a) for the first 25 components and in (b) for all components. In (a), individual values of E01 and E03 and of those of other subjects are shown with red and black dots, respectively. Error bars denote 95% CIs among the subjects. In (b), the horizontal axis is shown in log space for visibility. Consistent with the crossover evaluation for the training video, the projected correlation coefficients were especially high for the first several principal components. (c, d) The consistency of the inferred semantic vector for the validation video was tested using replicability across the four repetitions in the validation video. The inferred semantic vectors were projected to the direction vector of the PCA determined from the semantic vectors of the training video to calculate the correlation coefficients for all possible pairs across the repetitions. The correlation coefficients were Fisher z-transformed and averaged to be shown in (c) for the first 25 components and in (d) for all components. In (c), individual values of E01 and E03 and of those of other subjects are shown with red and black dots, respectively. Error bars denote 95% CIs among the subjects. In (d), the horizontal axis is shown in log space for visibility. For the first several principal components, the Fisher z-transformed correlation coefficients between the semantic vectors inferred from the high- γ features across the repeated 2.5-min videos were distributed at approximately 0.3–0.4.



Supplementary Fig. 5. Accuracy and modulation in the real-time feedback task. (a) Each plot shows the time course of real-time decoding accuracy. For each frame in the real-time feedback task, an online vector (v_{online}) used to determine the feedback image was evaluated as a three-choice task (three-choice accuracy). Dotted and dashed lines denote chance level (33.3%) and $P = 0.05$ false discovery rate-corrected significance levels, respectively. For the correction, the chance-level distribution of the three-choice accuracy with each frame was estimated by shuffling instructions of all trials 1 million times. (b, c) To elucidate how subjects controlled the inferred semantic vector during the real-time feedback task, modulation of the inferred vector depending on the instructed category (target category) was evaluated. During the real-time feedback task, the subjects viewed various images while visually imagining images representing the target category. For example, E01 viewed 124 different images commonly presented among three instructions; among them, 94 different images were included in the following analysis, avoiding overlaps of ECoGs corresponding

to the images by rejection of a portion of the frames. Frames to be rejected were selected using a generic algorithm with a criterion of maximizing the number of images included in this analysis. For each frame, ECoGs from 0 to 1 s after the presentation of the image was decoded ($v_{inferred}$) using high- γ features to calculate scene-wise correlation coefficients with each semantic vector of the instructions (direction: word, landscape, or human face) ($R(v_{inferred}, v_{word})$, $R(v_{inferred}, v_{landscape})$ and $R(v_{inferred}, v_{face})$), which then were Fisher z-transformed and frame-averaged among the same image with the same instructions (instruction) ($Z_{direction}^{instruction} := z(R(v_{inferred}, v_{direction}))$). In (b), the $Z_{direction}^{direction}$ for each image is shown on the vertical axis, where the average of two $Z_{direction}^{instruction}$ (instruction \neq direction) is shown on the horizontal axis by a marker coded with color corresponding to its first and second principal components (PCs) of the semantic vectors of the training video. The target categories are shown on the left. In (c), the modulation of the inferred semantic vector towards one of the instructions for each image (e.g., ΔZ_{word} for “word” instruction) is calculated as the differences of $Z_{direction}^{instruction}$ among instructions (e.g., $\Delta Z_{word} := Z_{word}^{word} - (Z_{word}^{landscape} + Z_{word}^{face}) / 2$; that is, the value on the vertical axis in (b) subtracted with that on the horizontal axis). The ΔZ_{word} or $\Delta Z_{landscape}$ showed large modulation, suggesting the subjects succeeded in increasing the $R(v_{inferred}, v_{word})$ or $R(v_{inferred}, v_{landscape})$ with the corresponding instruction during the real-time feedback task.



Supplementary Fig. 6. Image set for the imagery task and modulation of the inferred vector during the imagery task. (a) All images used in the imagery task are shown. Illustrations are presented instead of the actual images used in the task. (b) At the position of

the corresponding Pearson's correlation coefficients with the semantic vector (v_{word} or $v_{landscape}$), markers representing one single presentation of an image (0 to 1 s) were plotted with color coding (red, presentation of word image; orange, presentation of word image while visually imagining landscape; blue, presentation of landscape image; green, presentation of landscape image while visually imagining word). The histogram in the subplot shows the estimated distribution of the correlation coefficients shown in the same color using the normal kernel (band width = 0.02). *P*-values were calculated using uncorrected one-sided Welch's *t*-test performed on the Fisher z-transformed correlation coefficients ($n = 25$ for each group, except E09 whose $n = 50$). We calculated the scene-identification accuracy by comparing the inferred vector of each presented image in a non-imagery period against the corresponding true semantic vector of the presented image and the vectors of other images in the same category. The accuracy for the word category was $54.11 \pm 3.83\%$ (mean \pm 95% CIs among subjects); the accuracy for the landscape category was $50.28 \pm 4.57\%$. Replicability of the inferred semantic vectors in the non-imagery period was evaluated by calculating the Pearson's correlation coefficients for all possible pairs among presentations of the same image. The average of Fisher z-transformed correlation coefficients was 0.8619 ± 0.3308 (mean \pm 95% CIs among subjects) for the landscape images and 0.6443 ± 0.1722 for the word images. (c, d) For each 1-s time window, ECoGs were decoded using features from three frequency bands (α : 8–13 Hz; β : 13–30 Hz; low γ : 30–80 Hz) and combinations of them with the high- γ band to show (c) the area under the curve (AUC) to identify the category of the presented image in the non-imagery period (word or landscape) and (d) modulation. Individual values are shown with dots. Error bars denote 95% CIs among subjects ($n = 9$).

Supplementary Table 1. Number of electrodes for each cortical region.

	E01	E02	E03	E04	E05	E06	E07	E08	E09	E10	E11	E12	E13	E14	E15	E16	E17	E18	E19	E20	E21
Primary visual cortex (V1)	0	6	0	0	5	0	1	0	2	0	8	0	2	0	8	0	0	0	1	0	0
Early visual cortex (V2–V4)	0	14	5	0	16	0	6	0	4	0	12	5	7	0	15	2	0	4	7	0	0
Dorsal stream visual cortex	0	3	0	0	1	0	0	0	0	0	0	1	4	0	7	4	0	0	6	0	0
Ventral stream visual cortex	0	4	6	0	3	0	2	1	4	0	11	11	0	0	10	1	1	0	3	4	0
MT+ complex and neighboring visual areas	0	5	4	0	7	0	9	0	6	0	14	0	2	4	5	7	2	5	13	0	2
Somatosensory and motor cortex	2	0	0	2	0	3	0	3	2	2	0	0	14	2	0	9	1	1	0	11	1
Paracentral lobular and mid cingulate cortex	0	0	0	0	0	0	0	0	0	0	0	0	8	0	0	3	0	0	0	0	0
Premotor cortex	3	0	0	1	0	6	0	0	1	4	0	0	4	5	0	6	3	0	0	2	2
Posterior opercular cortex	1	0	0	2	0	1	0	1	4	1	0	2	0	6	0	0	2	1	0	3	2
Auditory association cortex	10	0	5	6	4	5	0	8	8	8	0	6	5	6	0	0	8	10	0	8	9
Medial temporal cortex	7	0	0	1	5	7	0	1	2	5	0	1	0	5	1	0	4	5	0	4	5
Lateral temporal cortex	29	9	13	23	31	18	7	22	33	17	5	20	5	27	4	4	24	33	6	28	23
Temporo-parieto-occipital junction	5	4	4	0	7	3	6	1	3	3	0	4	5	4	2	5	1	5	2	1	0
Superior parietal cortex	0	0	0	0	0	0	0	0	3	0	5	0	6	0	2	5	0	6	6	3	0
Inferior parietal cortex	4	17	13	2	1	7	5	3	27	6	10	4	16	6	12	25	6	8	5	14	1
Posterior cingulate cortex	0	2	0	0	2	0	0	0	0	0	11	2	0	0	2	1	0	0	1	0	0
Orbital and polar frontal cortex	4	0	0	0	0	0	0	0	0	2	0	0	0	0	0	0	0	2	0	0	0
Inferior frontal cortex	9	0	0	3	0	7	0	0	5	7	0	0	0	0	0	0	2	2	0	0	3
Dorsolateral prefrontal cortex	0	0	0	0	0	9	0	0	0	11	0	0	2	1	0	0	0	0	0	0	0
Depth	0	0	30	18	0	4	18	24	0	0	12	24	0	18	6	12	18	0	12	6	24

MT+ complex: middle temporal complex.

Supplementary Table 2. Words that have the highest and lowest correlation coefficients with principal components

Order of component	Top 10 words	Bottom 10 words
1 st	Male, Female, Wearing, Hairstyle, Blond hair, Older, Clothing, Wearing, Appearance, Girls	Terrain, Slope, Terrace, East side, North side, Gradient, Nearby, Hills, Landscape, Rainfall
2 nd	Climb, Walking, Foot, Lake, Sea, Mountaintop, Snow, Mountain, Cliff, Slope	Text ¹ , Text ² , Write, Display, Screen, Explicit, Telop, Font, Input, Logo
3 rd	Same building, Construction, Accommodation, Neighborhood, Relocation, City, Resident, Immigration, Building, Government	White, Black, Red, Yellow ³ , Light blue, Color, Green, Blue, Hair, Yellow ⁴
4 th	Look, Feel, Expression, Feeling, Capturing, Dark, Gentle, Looking, Impression, Understanding	Furniture, Confectionery, Supplies, Shop, Cooking, Selling, Table, Restaurant, Dish, Box lunch
5 th	<i>No</i> ⁵ , What, Say, Self, to be able to do, to do, to eat, to eat, to be troubled	Keys, Color ² , Logo, Middle, Men, Light blue, Gothic, Costume, Color ⁶ , Uniform
6 th	Front, Both sides, Rear, Back, Inner, Head, Mounting, Outer, Top, Back	Fun, Happy, Girls, Friends, Themes, I, Loving, Singing, Loving, Boys
7 th	Window, Table, Room, Ceiling, Sitting, Bed, Stairs, Chair, Entrance, Door	Conflict, Force, Capture, Strength, Arrest, Weapon, Defeat, Exercise, Guerrilla, Led
8 th	Writing ⁷ , Mountain, Mountains, Foot, Tradition, Writing ⁷ , Descending, Pass, Altitude, Tributary	Earth, Spacecraft, Space, Infrared, Room, Planet, Glowing, Solar system, Liquid crystal, Camera
9 th	Male, Female, Fish ⁸ , Fish ⁸ , Ocean, Edible, Collection, Seawater, Food, Extraction	Cry, Go home, Boy, Walk, Come, Go, I, You, Ask, When
10 th	Wearing ⁷ , Clothes, Clothing, <i>No</i> ⁵ , Uniform, Think ⁷ , Think ⁷ , Know, Reason, Wearing ⁷	Character (in book, film, etc.), Crash, Animation, Draw, Mecha, Drawing, Fish, Shoot, Illustration, Robot

From the text corpus used to train the skip-gram model, the most frequent 10,000 words were selected as candidates; their vector representations were tested by Pearson's correlation coefficients with the first 10 principal components of the true semantic vectors. ¹ In Kanji characters; ² In Katakana characters; ³ Noun; ⁴ Adjectives; ⁵ Japanese particles; ⁶ Not translated because word was in learned English; ⁷ Translated from different Japanese verbs; ⁸ Translated from different Japanese nouns.

Supplementary Table 3-1. Confusion matrix at the time point when classification accuracy peaked in the real-time feedback task for E01

		Predicted		
		Word	Landscape	Human face
Instruction	Word	26	6	8
	Landscape	10	24	6
	Human face	18	9	13

Supplementary Table 3-2. Confusion matrix at the time point when classification accuracy peaked in the real-time feedback task for E02

		Predicted		
		Word	Landscape	Human face
Instruction	Word	16	16	8
	Landscape	5	28	7
	Human face	2	14	24

Supplementary Table 3-3. Confusion matrix at the time point when classification accuracy peaked in the real-time feedback task for E03

		Predicted		
		Word	Landscape	Human face
Instruction	Word	25	10	5
	Landscape	10	17	13
	Human face	12	13	15

Supplementary Table 3-4. Confusion matrix at the time point when classification accuracy peaked in the real-time feedback task for E04

		Predicted		
		Word	Landscape	Human face
Instruction	Word	17	21	2
	Landscape	5	34	1
	Human face	9	24	7